

1 STAR Analysis Note:  
2 Measurement of transverse polarization of  $\Lambda$  in unpolarized  $pp$   
3 collision at 200GeV

4 Taoya Gao, Qinghua Xu, Yi Yu, and Jinlong Zhang

5 January 25, 2025

6 **Contents**

7	<b>1 Dataset</b>	<b>6</b>
8	<b>2 <math>\Lambda/\bar{\Lambda}</math> reconstruction</b>	<b>6</b>
9	<b>3 <math>V_0</math> jet reconstruction</b>	<b>7</b>
10	3.1 Modification of jet reconstruction . . . . .	10
11	3.2 Anti-proton annihilation correction . . . . .	10
12	3.3 Underlying events correction . . . . .	12
13	<b>4 MC Simulation</b>	<b>14</b>
14	4.1 Parameters set . . . . .	14
15	4.2 Particle identification correction . . . . .	14
16	4.3 Comparison of pure MC and data . . . . .	16
17	<b>5 Mixed Events</b>	<b>17</b>
18	5.1 The research of Mixed-event methods . . . . .	18
19	5.2 Closure test in MC . . . . .	22
20	5.3 Mixed-events sample . . . . .	28
21	<b>6 Transverse polarization <math>P_{\Lambda/\bar{\Lambda}}</math> extraction of <math>\Lambda/\bar{\Lambda}</math></b>	<b>32</b>
22	6.1 Detector acceptance correction . . . . .	32
23	6.2 Zero-test with $K_s^0$ . . . . .	36
24	6.3 Comparison of results extracted by mixed events and MC . . . . .	37
25	<b>7 Systematic uncertainties</b>	<b>37</b>
26	7.1 Trigger Bias . . . . .	38
27	7.2 Mixed event method . . . . .	38
28	7.3 Background estimation . . . . .	38
29	7.4 Decay parameter . . . . .	40
30	<b>8 Results and conclusion</b>	<b>42</b>
31	8.1 $P_{\Lambda/\bar{\Lambda}}$ vs jet $p_T$ . . . . .	42
32	8.2 $P_{\Lambda/\bar{\Lambda}}$ vs $z$ and $j_T$ . . . . .	42

33	8.3 Conclusions . . . . .	44
34	<b>References</b>	<b>46</b>
35	<b>Appendices</b>	<b>47</b>

## 36 List of Figures

37	1.1	distribution of the primary vertex $z$ . . . . .	7
38	2.1	(Left) particle identification of TPC by $dE/dx$ , (Right) the schematic of $\Lambda$ reconstruction. . . . .	8
39			
40	2.2	The invariant mass distribution of reconstructed $\Lambda$ . . . . .	9
41	3.1	The $\Lambda$ jet reconstruction process, where dashed black lines inside cone denote daughter tracks: $p, \pi$ that will be excluded from particle list. The red rectangle means tower energy deposited in BEMC or EEMC. The big blue arrow indicates the reconstructed jet direction. . . . .	10
42			
43			
44			
45	3.2	Comparison of tower energy of $p$ and $\bar{p}$ matched to BEMC or EEMC. . . . .	11
46	3.3	Tower map of BEMC that $p$ and $\bar{p}$ matched. . . . .	11
47	3.4	Comparison of $3 \times 3$ tower energy of $p$ and $\bar{p}$ matched to BEMC or EEMC. . . . .	12
48	3.5	Diagram of Off-axis method. . . . .	12
49	3.6	Underlying events $p_T$ and average UE $p_T$ versus number of jets. . . . .	13
50	3.7	Underlying events $p_T$ and average UE $p_T$ versus number of jets. . . . .	13
51	4.1	Jet contributions from different ptHard ranges. . . . .	15
52	4.2	$n\sigma$ distributions of proton in data and MC sample . . . . .	15
53	4.3	$dE/dx$ vs momentum distributions of proton in data and MC sample . . . . .	16
54	4.4	Left: 2-dimensional distribution of proton $n\sigma$ as a function of momentum ; Right: the mean value of $n\sigma_p$ versus proton momentum . . . . .	17
55			
56	5.1	Mixed event procedure . . . . .	18
57	5.2	Azimuth phase space . . . . .	18
58	5.3	The near-jet mixed events . . . . .	19
59	5.4	The off-jet mixed events . . . . .	19
60	5.5	Top panel: comparisons of jet $p_T$ between SE and random ME; Bottom panel: comparisons of jet $p_T$ between SE and near-jet ME . . . . .	20
61			
62	5.6	Top panel: comparisons of $z$ between SE and random ME; Bottom panel: comparisons of $z$ between SE and near-jet ME . . . . .	20
63			
64	5.7	Top panel: comparisons of $j_T$ between SE and random ME; Bottom panel: comparisons of $j_T$ between SE and near-jet ME . . . . .	21
65			
66	5.8	Comparison of $\cos\theta^*$ between random and near-jet mixed event . . . . .	21
67	5.10	Left: $\Delta R$ vs $z$ of $\Lambda$ at mixed events. Right: $\Delta R$ vs $z$ of $\Lambda$ at same events . . . . .	22
68	5.9	Comparison of $\Delta R, z, j_T$ distribution of $\Lambda$ between SameEvents and MixedEvents before reweighting. . . . .	23
69			
70	5.11	Comparison of $\Delta R, z, j_T$ distribution of $\Lambda$ between same events and mixed events after reweighting. . . . .	24
71			
72	5.12	Comparison of $\Lambda p_T$ distribution between same events and mixed events. . . . .	25
73	5.13	Comparison of $\Lambda \eta$ distribution between same events and mixed events. . . . .	25
74	5.14	Comparison of $\Lambda \phi$ distribution between same events and mixed events. . . . .	26
75	5.15	Comparison of $\cos\theta^*$ of $\Lambda$ between same events and mixed events. . . . .	26
76	5.16	Left: $\cos\theta^*$ of $\Lambda$ at particle level. Right: $\cos\theta^*$ of $\Lambda$ at detector level . . . . .	27
77	5.17	Extracted polarization vs input polarization of $\Lambda, \bar{\Lambda}$ and $K_s^0$ . . . . .	27
78	5.18	Left: $\Delta\eta$ vs $\eta_{jet}$ in mixed events. Right: $\Delta\eta$ vs $\eta_{jet}$ in same events. . . . .	28
79	5.19	Comparisons of three kinematic quantities $p_T, \eta, \phi$ of $\Lambda$ and jet between SE and ME. . . . .	29
80			
81	5.20	Comparisons of three kinematic quantities $p_T, \eta, \phi$ of $\bar{\Lambda}$ and jet between SE and ME. . . . .	30
82			

83	5.21	Comparisons of $\Delta R, z, j_T$ of $\Lambda$ between SE and ME. . . . .	31
84	5.22	Comparisons of $\Delta R, z, j_T$ of $\bar{\Lambda}$ between SE and ME. . . . .	31
85	5.23	Comparisons of $\Delta R, z, j_T$ of $K_s^0$ between SE and ME. . . . .	32
86	6.1	$\cos\theta^*$ distribution of $\Lambda$ for the same event(left) and mixed events(right) . . . . .	32
87	6.2	$\cos\theta^*$ distribution of $\Lambda$ after acceptance correction and was fitted with a linear	
88		function (red line) to extract polarization . . . . .	33
89	6.3	Extraction of transverse polarization of $\Lambda$ as a function of jet $p_T$ . . . . .	34
90	6.4	Extraction of transverse polarization of $\bar{\Lambda}$ as a function of jet $p_T$ . . . . .	35
91	6.5	Transverse polarization of $K_s^0$ as a function of jet $p_T$ . . . . .	36
92	6.6	Transverse polarization of $K_s^0$ as a function of $z$ at different jet $p_T$ ranges . . . . .	36
93	6.7	Transverse polarization of $K_s^0$ as a function of $j_T$ at different jet $p_T$ ranges . . . . .	37
94	6.8	Transverse polarization extracted by MC . . . . .	37
95	6.9	Transverse polarization extracted by mixed events . . . . .	37
96	7.1	Flavor fraction distribution of $\Lambda$ at different jet $p_T$ . . . . .	38
97	7.2	Relative change between inputted and extracted polarization. . . . .	39
98	7.3	The extracted $\Lambda$ polarization under varied side-band shift. The top two panels	
99		show polarization extraction under left shift of side-band, the bottom two panels	
100		show the polarization extraction under right shift of side-band. . . . .	40
101	8.1	Transverse polarization of $\Lambda$ and $\bar{\Lambda}$ as a function of jet $p_T$ in unpolarized $pp$	
102		collisions at $\sqrt{s}=200$ GeV at STAR. Statistical uncertainties are shown as vertical	
103		bars. Systematic uncertainties are shown as boxes. . . . .	42
104	8.2	Transverse polarization of $\Lambda$ ,and $\bar{\Lambda}$ as a function of $z$ at different jet $p_T$ ranges	
105		of $6 < p_T^{jet} < 8.4$ GeV (left), $8.4 < p_T^{jet} < 12$ GeV (middle) and $p_T^{jet} > 12$	
106		GeV (right). Statistical uncertainties are shown as vertical bars. Systematic	
107		uncertainties are shown as boxes. . . . .	43
108	8.3	Transverse polarization of $\Lambda$ ,and $\bar{\Lambda}$ as a function of $j_T$ at different jet $p_T$ ranges	
109		of $6 < p_T^{jet} < 8.4$ GeV (left), $8.4 < p_T^{jet} < 12$ GeV (middle) and $p_T^{jet} > 12$	
110		GeV (right). Statistical uncertainties are shown as vertical bars. Systematic	
111		uncertainties are shown as boxes. . . . .	44

112 **List of Tables**

113	1.1	Dataset in this analysis. . . . .	6
114	1.2	Triggers used in the analysis . . . . .	6
115	2.1	The table of $\Lambda(\bar{\Lambda})$ topological cuts at different $p_T$ ranges . . . . .	8
116	2.2	The table of $K_s^0$ topological cuts at different $p_T$ ranges . . . . .	8
117	5.1	The table of $\Lambda$ extracted polarization and input polarization . . . . .	27
118	7.1	The table of $\Lambda$ extracted polarization, statistical uncertainties and summary of	
119		systematic uncertainties at different jet $p_T$ ranges . . . . .	41
120	7.2	The table of $\bar{\Lambda}$ extracted polarization, statistical uncertainties and summary of	
121		systematic uncertainties at different jet $p_T$ ranges . . . . .	41
122	8.1	The table of $\Lambda$ and $\bar{\Lambda}$ extracted polarization, statistical uncertainties and summary	
123		of systematic uncertainties at different jet $p_T$ ranges . . . . .	43
124	8.2	The table of $\Lambda$ and $\bar{\Lambda}$ extracted polarization, statistical uncertainties and summary	
125		of systematic uncertainties at different $z$ ranges . . . . .	44
126	8.3	The table of $\Lambda$ and $\bar{\Lambda}$ extracted polarization, statistical uncertainties and summary	
127		of systematic uncertainties at different $z$ ranges . . . . .	45

# 1 Dataset

The data set (summarized in Table 1.1) used in this analysis includes pp200long\_2015, pp200long2\_2015 and pp200trans\_2015 at present, which were taken in RHIC-STAR at  $\sqrt{s} = 200$  GeV in pp collision with 689, 557 and 686 good physics runs respectively. The sum of the integrated luminosity of the three samples is about  $133 \text{ pb}^{-1}$ . Jet-Patch triggers(JP1, JP2), as shown in Table.1.2, are used in the analysis.

System and energy	<i>pp collisions at <math>\sqrt{s} = 200</math> GeV</i>		
Data	pp200long_2015	pp200trans_2015	pp200long2_2015
Number of run	689	686	557
Total events	436 M	862 M	728 M
Luminosity( $\text{pb}^{-1}$ )	29	52	52
Production	P16id		
Trigger	JP1(470404, 480404, 480414, 490404) JP2(470401, 480401, 480411, 490401)		

Table 1.1: Dataset in this analysis.

Trigger	ID	Threshold (ADC channels)	Equivalent $E_T$ (GeV)
JP1	490404	28	5.4
JP2	490401	36	7.3

Table 1.2: Triggers used in the analysis

Some sub-detectors of STAR such as the TPC, BEMC, and EEMC are used in this analysis. The Events with primary vertex  $z$  within  $\pm 90$  cm from the center of TPC along the beam direction are selected. The primary vertex rank must be larger than  $10e6$ , with about  $5.93 \times 10^8$  events after  $z$  cuts. Fig. 1.1 showed the primary vertex  $z$  distribution before the selection of primary vertex  $z$ .

## 2 $\Lambda/\bar{\Lambda}$ reconstruction

The  $\Lambda$  hyperon characterized by self-analyzing weak decay has played a special role in the field of spin physics [1]. The  $\Lambda(\bar{\Lambda})$  candidates are reconstructed via the weak decay channel:  $\Lambda \rightarrow p + \pi^-$  ( $\bar{\Lambda} \rightarrow \bar{p} + \pi^+$ ), following a similar procedure as in Ref. [2] except that the Time of Flight (TOF) hit matching is not required for the pion track. Firstly, good-quality tracks are obtained by following criteria:

- Track flag:  $0 \sim 1000$

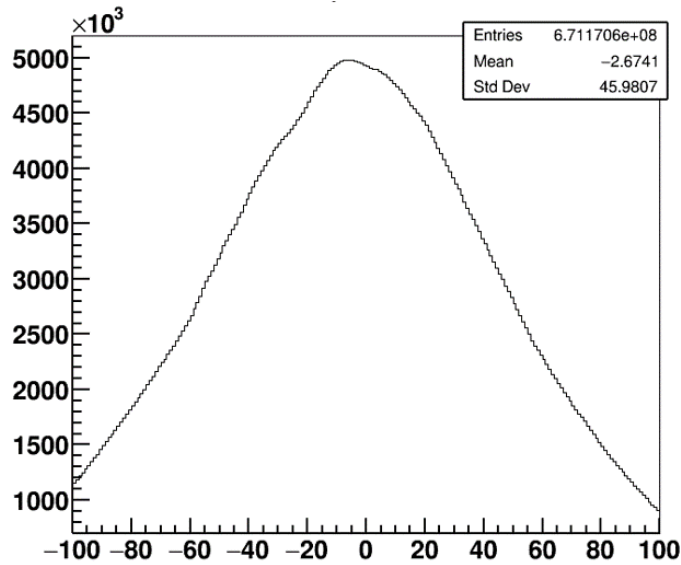


Figure 1.1: distribution of the primary vertex  $z$ .

- 146 •  $p_T := > 0.15 \text{ GeV}$
- 147 •  $\text{NHits} > 15$
- 148 •  $\text{NHits}/\text{NHitsPoss} > 0.52$
- 149 •  $\text{DCA} < 30 \text{ cm}$

150 The TPC detector provides charge tracking and particle identification, which is used to select  
 151 protons and  $\pi$  from a bunch of particles by ionization energy loss  $dE/dx$ . Because of the  
 152 limited resolution of TPC detector, the capability of particle identification is reduced for charge  
 153 particles with large momentum that are shown in Fig.2.1 (a) [3] that present ionization energy  
 154 loss of four type particles,  $e^\pm$ ,  $p(\bar{p})$ ,  $\pi^\pm$  and  $K^\pm$ . The  $n\sigma$  cut of proton candidate, for example,  
 155 was required to be within  $\pm 3\sigma$  to the theoretical values of  $dE/dx$  for proton. This cut is  
 156 a reasonable value to balance the statistics and particle identification quality. Two daughter  
 157 tracks with opposite charges are paired and hyperon  $p_T$ -dependent topological selection criteria,  
 158 summarized in Tab.2.1 and 2.2, are applied to suppress the background with an acceptable  
 159 percentage of about 10%. Figure 2.2 shows the invariant mass distribution of  $\Lambda$ .

### 160 3 $V_0$ jet reconstruction

161 In order to implement the measurement of  $\Lambda$  polarization contribution from the fragmentation  
 162 process, we need to reconstruct jet. The momentum direction of jet will be regarded as the  
 163 direction of the fragmenting parton. This is also critical to determine the polarization direction  
 164 of  $\Lambda$ . In this analysis, the jet was reconstructed with anti- $k_T$  algorithm with following parameter  
 165 sets.

- 166 • Reconstruction: anti- $k_T$  with  $R = 0.6$
- 167 • Tracks: primary track with  $p_T > 0.2 \text{ GeV}$  and  $\text{DCA} < 3 \text{ cm}$
- 168 • Towers are required to have  $E_T > 0.2 \text{ GeV}$

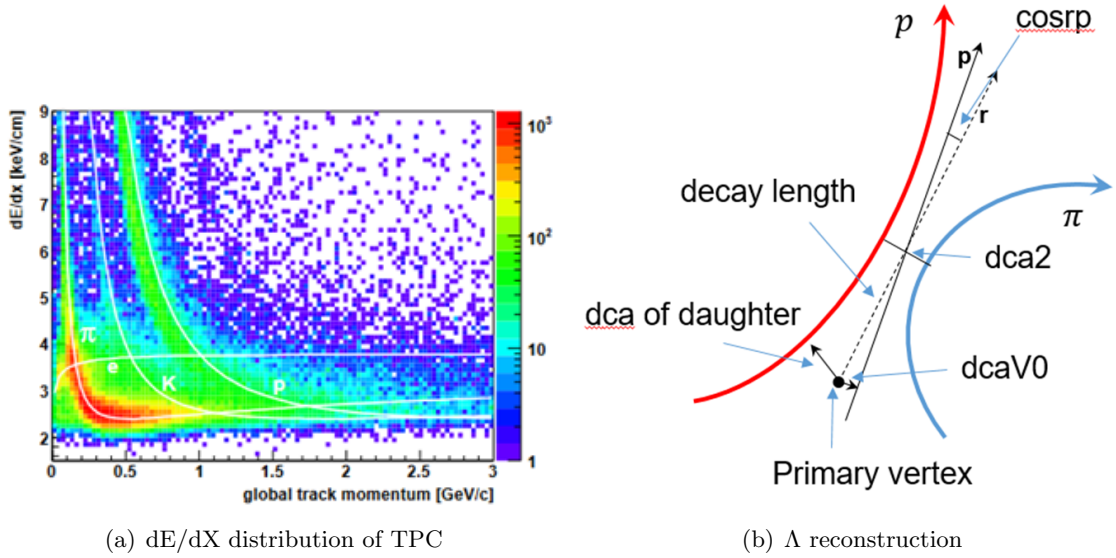


Figure 2.1: (Left) particle identification of TPC by dE/dx, (Right) the schematic of  $\Lambda$  reconstruction.

$\Lambda(\bar{\Lambda})$ topological cuts							
$p_T$ [GeV/c]	0 – 1	1 – 2	2 – 3	3 – 4	4 – 5	5 – 6	> 6
$ n\sigma  <$	1.5	1.5	1	1	1	1	1
$DCA2(cm) <$	0.65	0.65	0.60	0.55	0.50	0.45	0.40
$DCA_p(cm) >$	0.45	0.35	0.30	0.15	0.005	0.005	0.005
$DCA_\pi(cm) >$	0.65	0.65	0.60	0.55	0.50	0.50	0.50
$DCAV0(cm) <$	0.55	0.65	0.75	1.0	1.0	1.0	1.0
$DecayLength(cm) >$	3.0	3.0	3.5	3.5	4.0	4.5	4.5
$cosrp >$	0.995	0.995	0.995	0.995	0.995	0.995	0.995

Table 2.1: The table of  $\Lambda(\bar{\Lambda})$  topological cuts at different  $p_T$  ranges

$K_s^0$ topological cuts							
$p_T$ [GeV/c]	0 – 1	1 – 2	2 – 3	3 – 4	4 – 5	5 – 6	> 6
$ n\sigma  <$	1.35	1.35	1.35	1.40	1.45	1.50	1.70
$DCA2(cm) <$	0.65	0.65	0.65	0.55	0.55	0.50	0.35
$DCA_p(cm) >$	0.60	0.55	0.50	0.35	0.30	0.25	0.20
$DCA_\pi(cm) >$	0.60	0.55	0.50	0.35	0.30	0.25	0.20
$DCAV0(cm) <$	0.65	0.70	0.80	0.90	0.90	0.90	0.90
$DecayLength(cm) >$	3.55	3.60	3.70	3.75	3.80	4.0	5.5
$cosrp >$	0.995	0.995	0.995	0.995	0.995	0.995	0.995

Table 2.2: The table of  $K_s^0$  topological cuts at different  $p_T$  ranges



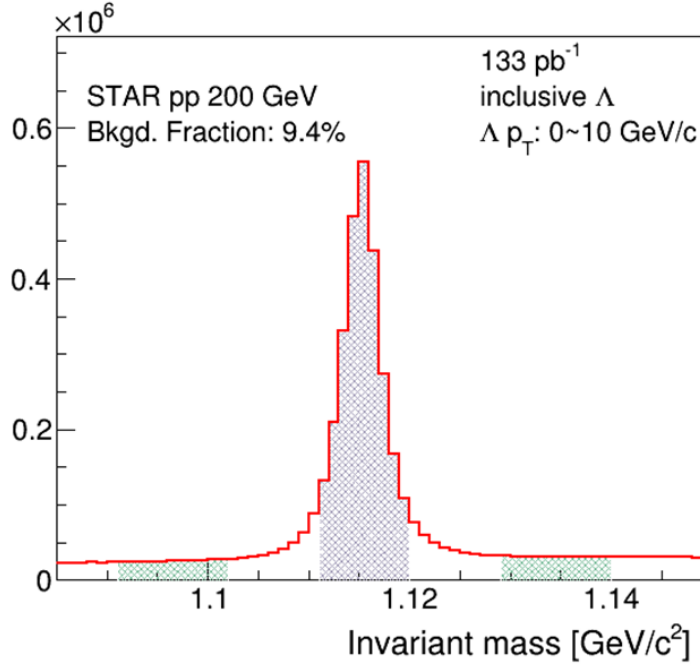


Figure 2.2: The invariant mass distribution of reconstructed  $\Lambda$  .

- 169     • The jet  $p_T > 5$  GeV  
 170     • Anti-proton energy correction

171 The final production of the whole fragmentation process consists of a variety of charge particles  
 172 and neutral particles. We aim to probe the  $\Lambda$  polarization in final states. Therefore, the jets used  
 173 here is full-jet consisting of both charge tracks from TPC and neutral energy from EEMC and  
 174 BEMC. Only primary tracks with  $DCA < 3cm$  are utilized for jet reconstruction. To reduce noise  
 175 background, the track  $p_T$  and tower energy  $E_T$  are required to be larger than 0.2 GeV. In case  
 176 of the additional energy deposits in detector from possible annihilation effects of  $\bar{p}$  with proton  
 177 from material of BEMC and EEMC, the  $\bar{p}$  annihilation correction is necessary(see Section 3.2).  
 178 Besides, to reduce the other effects from underlying events (UE), we applied off-axis method to  
 179 do the UE corrections, which helps to reduce the pile-up events. The jet candidates satisfying  
 180 follow selection cuts are considered in this analysis.

- 181     • Jet  $p_T - UE p_T > 5$  GeV and pass trigger threshold  
 182     • Neutral fraction  $R < 0.95$   
 183     • Jet  $\eta$ :  $-1 < \eta < 1$   
 184     • Jet detector  $\eta_{det}$ :  $-0.7 < \eta_{det} < 0.9$

185 The goal of neutral fraction  $R < 0.95$  requirements is to avoid the contribution from charge  
 186 tracks of TPC is too low. The difference between jet  $\eta$  and detector  $\eta_{det}$  is that  $\eta_{det}$  indicates  
 187 the pseudorapidity of tower position in EMC relative to the TPC center.

188 **3.1 Modification of jet reconstruction**

189 Unlike traditional jet reconstruction in STAR, in this analysis, the reconstructed  $\Lambda/\bar{\Lambda}$  candidates  
 190 will also be added to the input list for jet reconstruction. Meanwhile, the primary tracks  
 191 associated with the  $\Lambda/\bar{\Lambda}$  daughter tracks will be excluded to avoid double counting. The diagram  
 192 of this process is presented in Fig. 3.1. In some cases,  $\Lambda/\bar{\Lambda}$  and  $K_S^0$  may share the same daughter  
 193 track due to the misidentification between protons and pions. This effect will introduce potential  
 194 double counting if  $\Lambda/\bar{\Lambda}$  and  $K_S^0$  are both added to the same input list for jet reconstruction. To  
 195 avoid such double counting, the  $\Lambda/\bar{\Lambda}$ -jets and  $K_S^0$ -jets were reconstructed separately.

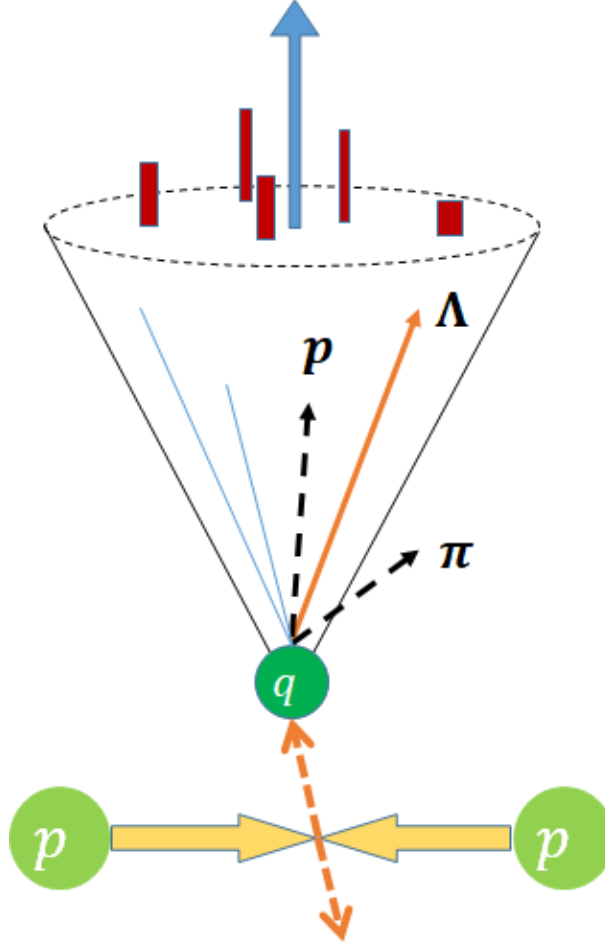


Figure 3.1: The  $\Lambda$  jet reconstruction process, where dashed black lines inside cone denote daughter tracks:  $p, \pi$  that will be excluded from particle list. The red rectangle means tower energy deposited in BEMC or EEMC. The big blue arrow indicates the reconstructed jet direction.

196 **3.2 Anti-proton annihilation correction**

197 The annihilation effects of antiproton produced in the final state with materials of BEMC/EEMC  
 198 are non-negligible. For example, the  $\bar{p}$  decayed from  $\bar{\Lambda}$ , especially for low momentum, would  
 199 likely annihilate with protons from BEMC/EEMC materials and deposit additional energy in  
 200 BEMC/EEMC. This additional energy will also impact the neutral fraction in the process of  
 201 jet reconstruction and increase the original actual jet energy. Fig.3.2 displays the tower energy

202 distribution deposited in BEMC and EEMC that match to  $p$  and  $\bar{p}$ . According to parity con-  
 203 servation, the behaviors of  $p$  and  $\bar{p}$  should be similar, which are different from the results in the  
 204 plots. There is an apparent enhancement at large tower energy for  $\bar{p}$ . And the mean value of  
 205 proton tower energy is 0.6 GeV, even only about half of that for  $\bar{p}$ .

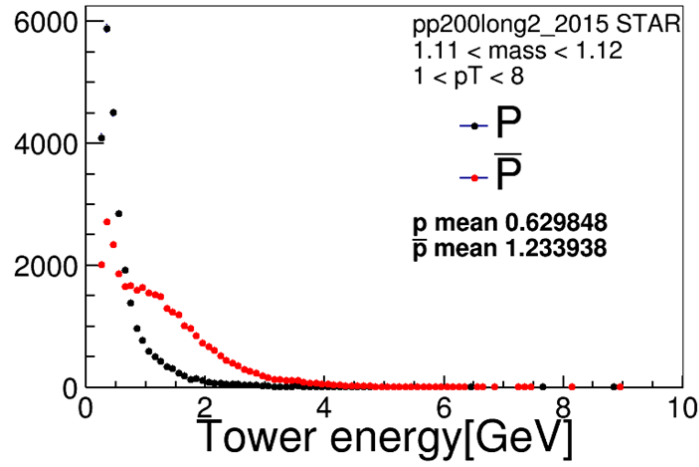


Figure 3.2: Comparison of tower energy of  $p$  and  $\bar{p}$  matched to BEMC or EEMC.

206 Nevertheless, the deposited energy of  $\bar{p}$  was still less than the theoretical value (twice of proton  
 207 mass), if annihilated with other detector protons. One of the reasons we suppose might be that  
 208 the additional energy extended to surrounding towers, which caused the tower energy matched  
 209 to  $\bar{p}$  shift to the low energy range. To include annihilation energy of  $\bar{p}$  deposited in calorimeters  
 210 as much as possible, the tower region matched to charge particle expands from one tower to  
 211 surrounding 9 towers. As shown in Fig.3.3, the number denotes the tower index in detectors  
 212 within the phase space constructed by  $\eta$  and  $\phi$  axis.

213 Significantly, the energy distribution including 9 towers matched to  $\bar{p}$  shifts to the large value  
 214 range with a peak at about 2 GeV. At the same time, No significant changes were observed for  $p$ .  
 215 Such results demonstrate that the annihilation effects of  $\bar{p}$  can not be ignored and it is necessary  
 216 to make corrections. In this analysis,  $3 \times 3$  towers energy with it central tower matched to  $\bar{p}$  are  
 217 removed from the jet reconstruction.

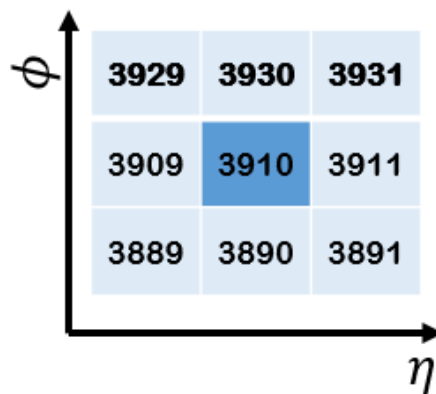


Figure 3.3: Tower map of BEMC that  $p$  and  $\bar{p}$  matched.

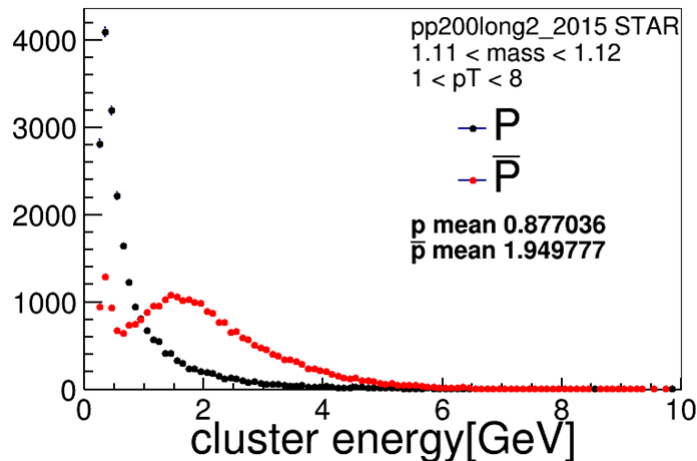


Figure 3.4: Comparison of  $3 \times 3$  tower energy of  $p$  and  $\bar{p}$  matched to BEMC or EEMC.

### 218 3.3 Underlying events correction

219 The typical method, off-axis cone[4], was used in this analysis to subtract contributions from  
 220 underlying events (UE), which contribute mostly low  $p_T$  tracks. They are corresponding to all  
 221 particles produced directly from pile-up or hard scattering of partons, which are regarded as  
 222 the contamination of jet. The two cones with the same  $\eta$  as jet, but perpendicular to the jet  
 223 cone, are adopted to evaluate the UE particle yield. As shown in Fig. 3.5, the UE cones, dashed  
 224 circular line with the radius equal to the jet resolution parameter ( $R = 0.6$ ), are offset by an  
 225 azimuthal angle  $\phi = \pi/2$  with respect to the jet axis.

226 A general strategy for the UE contamination correction is to subtract the UE contribution to  
 227 the jet  $p_T$  jet-by-jet. The  $p_T$  spectra of all particles inside these two UE cone are accumulated  
 228 and divided by cone area, namely  $2\pi R^2$ , to obtain the UE  $p_T$  density  $\rho$ . Hence, the average  
 229 UE  $p_T$  could be obtained through  $\rho \times A_{jet}$ , where  $A_{jet}$  is the area of the jets calculated by the  
 230 Fastjet package[5].

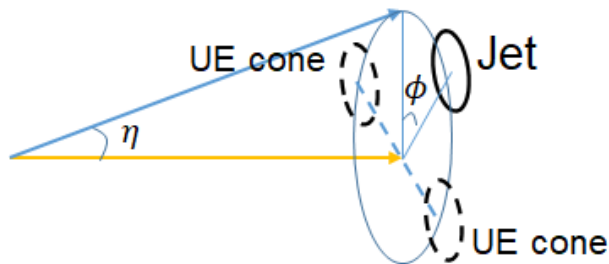


Figure 3.5: Diagram of Off-axis method.

231 However, in the multi-jet events, two or more jets with the same  $\eta$  but the  $\Delta\phi = \pi/2$  probably  
 232 occurred in the same event. It means the UE contribution to the jet  $p_T$  would be significantly  
 233 overestimated, which will enhance the UE  $p_T$ . Figure 3.6 shows the UE  $p_T$  spectra with jet  
 234 number dependence, and the average UE  $p_T$  increases with jet numbers. As a result, the jet  $p_T$   
 235 will be over corrected, if using these raw UE  $p_T$  that was enhanced by contribution from a real  
 236 jet. What we did for this issue is to modify the UE region selection by including a protection

237 that when a jet was found nearby UE cones ( $\Delta R \leq 1.2$ ), particles in that UE cones will be  
 238 excluded from the UE  $p_T$  calculations.

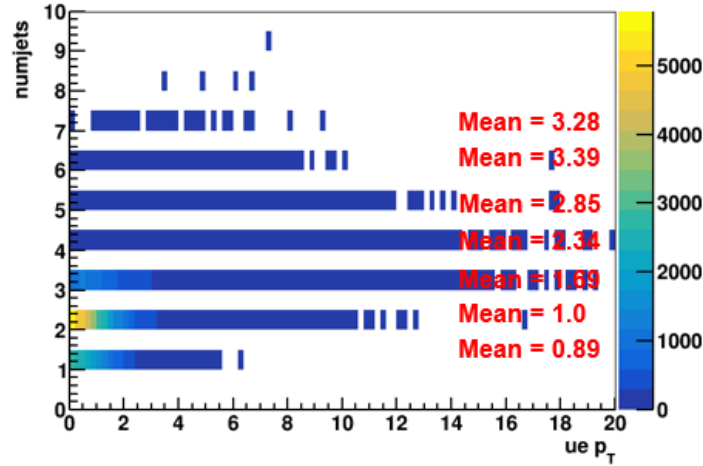


Figure 3.6: Underlying events  $p_T$  and average UE  $p_T$  versus number of jets.

239 The threshold of the jet that was regarded as a jet found nearby UE cones is set as 4 GeV.  
 240 Following plots, Fig. 3.7, show the UE results after applying a protection mechanism in two  
 241 UE cones. Apparently, this protection mechanism impacts largely on the UE  $p_T$  calculations,  
 242 especially for multi-jets events. On the other hand, the threshold setup of a jet is also a crucial  
 243 factor. Lower threshold means a jet would be identified as a real jet easier. See for the two plots  
 244 of Fig. 3.7, the different minimum jet  $p_T$  are 4 GeV and 2.5 GeV respectively and resulted in  
 245 different average UE  $p_T$ . In the left plot, the label ‘3coneUE’ denotes another cone at opposite  
 246 azimuth relative to the jet was regarded as UE cone either, which aimed to compensate the  
 247 deficiency of UE cone resulted by protection mechanism but was canceled at final analysis. To  
 248 keep things consistent, all parameters of jet nearby UE cones are the same as jet parameters  
 249 above.

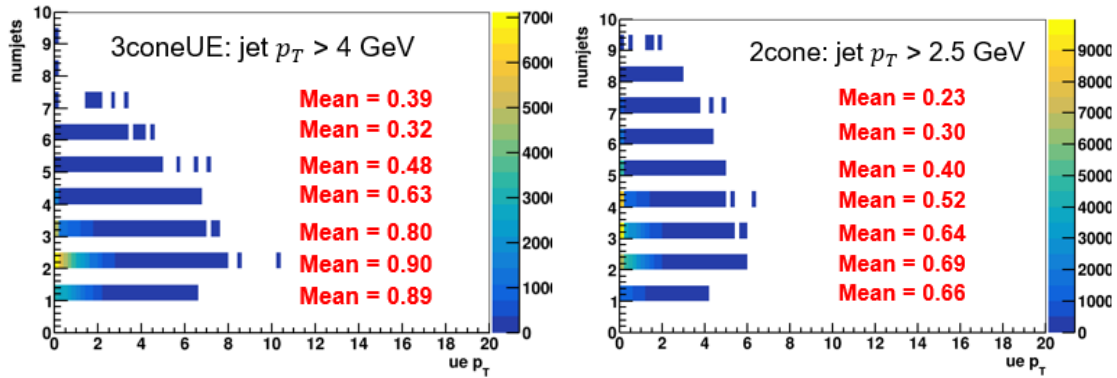


Figure 3.7: Underlying events  $p_T$  and average UE  $p_T$  versus number of jets.

## 4 MC Simulation

To correct acceptance effects from limited detector acceptance range and efficiency, we need to obtain acceptance functions corresponding to the STAR detector, which could be available by Monte Carlo (MC) simulation. There are many MC generators for the simulation of the pp collisions. In this analysis, simulation events are generated by PYTHIA6.4.28 [6] and then run through GEANT3 [7] based on STAR detectors.

### 4.1 Parameters set

The simulated events should be embedded into “zero-bias” data which was taken by triggered randomly in the period of run. Because these events with zero-bias trigger could be used to simulate beam background and pile-up events to make the simulation closer to the actual conditions. However, based on our study, we find it does not greatly affect the acceptance function without zero-bias data from simulation. The simulation setup are listed following:

- PYTHIA6.4.28 + GEANT3
- ptHard > 4 GeV
- Energy 200 GeV
- Geometry: y2015c
- $\Lambda/\bar{\Lambda}$  filter: promise every event include at least one  $\Lambda/\bar{\Lambda}$  with  $p_T > 0.5$  GeV
- Primary vertex: Gaussian distributions with  $\sigma_x = 0.026$  cm,  $\sigma_y = 0.015$  cm,  $\sigma_z = 41.48$  cm

The reason why ptHard is larger than 4 GeV, rather than the usual several separate regions from 2 to 35, is to increase simulation efficiency with jet-patch trigger as much as possible while suppress edge effects of trigger threshold as low as possible, simultaneously. Figure 4.1 shows the ratio of contributions of different ptHard ranges to jet  $p_T$  spectra. The left plot is for the JP1 trigger and the right one is for the JP2 trigger. The percentage of the contribution to jet  $p_T$  spectrum from ptHard 2 ~ 3 GeV is about 5.68% and from ptHard 3 ~ 5 GeV is about 7.53%. Moreover, the efficiency for a event from ptHard 2 ~ 4 GeV that passes trigger threshold is too low to obtain sufficient statistics within acceptable time duration. Therefore, 4 GeV is an appropriate value for minimum ptHard.

The goal of applying  $\Lambda/\bar{\Lambda}$  filter is to increase simulation efficiency and save disk space by selecting events that include at least one  $\Lambda$  or  $\bar{\Lambda}$  with  $p_T > 0.5$  GeV. For the JP1 and JP2 triggers, we also applied the trigger simulator to simulate the trigger response. The same algorithms as the data are applied in MC simulation to reconstruct  $\Lambda/\bar{\Lambda}$  and jet.

### 4.2 Particle identification correction

In the analysis, we encountered a severe issue with the MC sample: the central value of  $n\sigma$  distribution from the MC sample significantly deviated from its theoretical value and also differed from the real data distribution. The distributions of  $n\sigma$  for protons in both the MC and real data samples are shown below in Fig.4.2. The center of the proton  $n\sigma$  distribution in the MC sample is shifted towards negative values by approximately one sigma. In contrast, the center of the proton  $n\sigma$  distribution in the data sample is consistent with zero. This issue will introduce potential biases to the measurements as same  $n\sigma$  selection cuts were applied to both read data and MC samples.

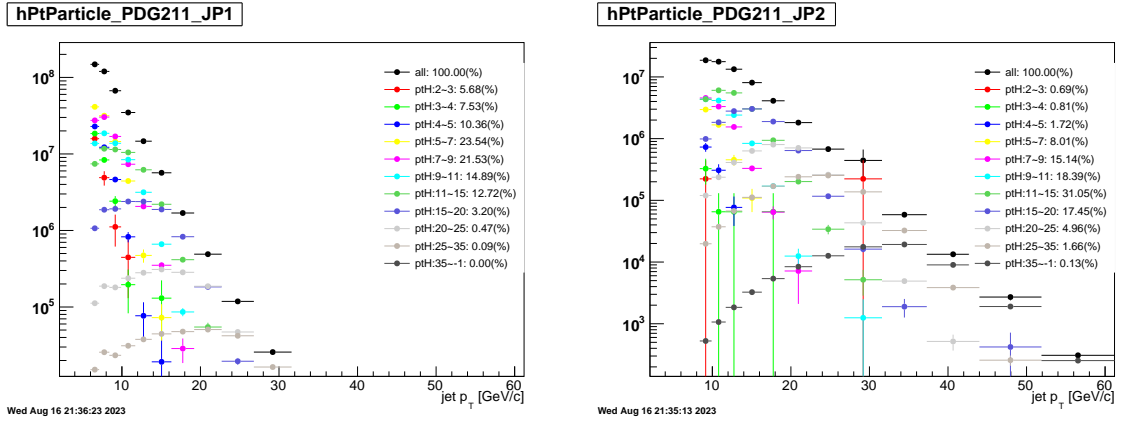


Figure 4.1: Jet contributions from different ptHard ranges.

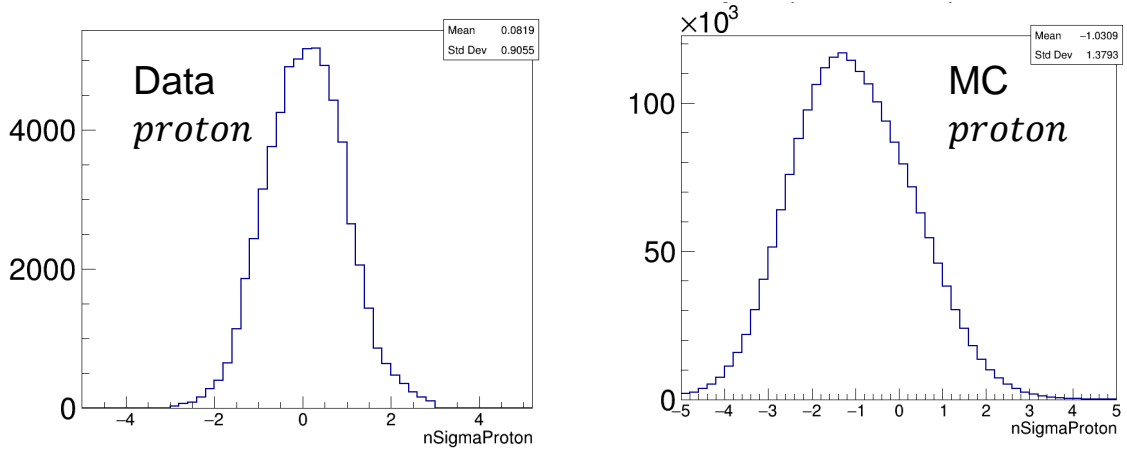


Figure 4.2:  $n\sigma$  distributions of proton in data and MC sample

290 Upon careful examination, we found that the cause of this phenomenon is due to inadequate  
 291 simulation of particle ionization energy loss in the gas during the generation of the MC sample.  
 292 The blue and green lines in the Fig. 4.3 below represent the fits to the ionization energy loss as a  
 293 function of momentum for protons at the detector level and association level in the MC sample,  
 294 respectively. These do not match the distribution of ionization energy loss versus momentum  
 295 for protons in the real data sample. Similar issues are observed for other types of particles as  
 296 well.

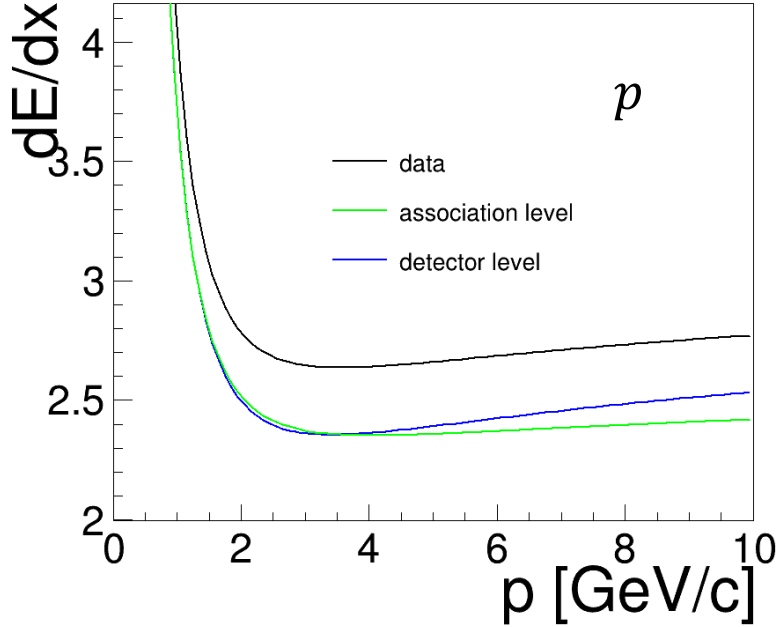


Figure 4.3:  $dE/dx$  vs momentum distributions of proton in data and MC sample

297 To avoid the bias introduced by suboptimal simulation of ionization energy loss, we must apply  
 298 a correction. The method involves fitting the distribution of the  $n\sigma$  mean values as a function  
 299 of momentum to ascertain the deviation from the theoretical curve. For this step, we require a  
 300 clean sample of particles, so we extracted particles at the association level, which are associated  
 301 directly with pure particles produced by PYTHIA. The left plot of Fig.4.4 shows a 2-dimensional  
 302 distribution of proton  $n\sigma$  as a function of momentum. And right plot is the distribution of  
 303 the mean value of  $n\sigma_p$  versus proton momentum, which shows a complex dependence. Then,  
 304 we subtract the corresponding deviation value from each particle's  $n\sigma$ , realigning it with the  
 305 theoretical value.

### 306 4.3 Comparison of pure MC and data

307 The reconstruction of  $\Lambda$ ,  $\bar{\Lambda}$ , and  $K_s^0$  in both MC and data employed identical reconstruction  
 308 methods, selection criteria, and topological cuts to ensure consistency. Comparisons of the data  
 309 and MC simulation are shown in the Appendices. We can find a good agreement for  $p_T$  between  
 310 the data and MC simulation.

311 For pseudo-rapidity  $\eta$  and azimuth angle  $\phi$ , some sectors of TPC issued this year resulted in  
 312 the nonuniform distributions of azimuth angle  $\phi$  and asymmetrical  $\eta$  distribution relative to  
 313 zero. However, MC simulation is not consistent with data, which means GEANT3 based on



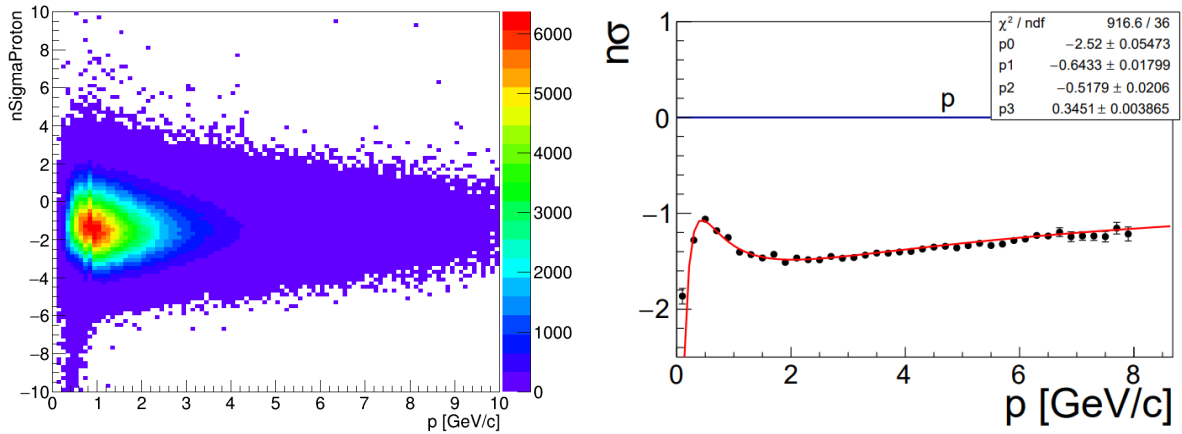


Figure 4.4: Left: 2-dimensional distribution of proton  $n\sigma$  as a function of momentum ; Right: the mean value of  $n\sigma_p$  versus proton momentum

314 the STAR detector did not simulate perfectly the true status of the STAR detector. These will  
 315 influence acceptance correction. Simultaneously, the statistic of the MC simulation sample is  
 316 highly hard to produce due to low efficiency and limited resources. We just utilize it to check  
 317 the new method of acceptance correction and estimate trigger bias.

## 318 5 Mixed Events

319 The biggest disadvantage of MC simulation is its statistics are still not enough for acceptance  
 320 correction of data, which resulted statistical uncertainty of results are too large to obtain a definite  
 321 conclusion. Thus, another alternative method, named mixed-event method[8], is proposed  
 322 for this analysis. This is a popular method utilized widely to estimate combination backgrounds  
 323 by mixing different tracks from randomly different events, the details can be found in reference  
 324 [8]. An important reason we want to use the mixed event method is its fast production and  
 325 smaller storage space, which could save lots of time and computer resources.

326 In this analysis, the mixed method is a little different but with the same principle. A recon-  
 327 structed  $\Lambda$  particle will be embedded into a different event to form a mixed event, then using  
 328 this event to reconstruct  $\Lambda$  jet. The procedures are shown in Fig.5.1. Of course, these two events  
 329 must be required with the same trigger and their discrepancy of primary vertex  $z$  is smaller than  
 330 5 centimeters, and mixed events must be applied to the individual run aiming to ensure similar  
 331 conditions as much as possible. Owing to there being no correlation between  $\Lambda$  and jet from  
 332 different events, no physic signal of polarization will be obtained theoretically, and the original  
 333 correlation between  $\Lambda$  and jet at the SE is also broken simultaneously.

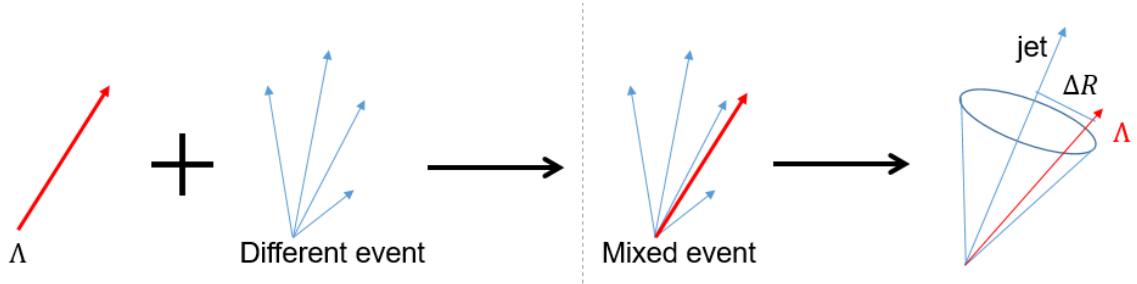


Figure 5.1: Mixed event procedure

### 334 5.1 The research of Mixed-event methods

335 There are two types of mixed events in this analysis based on constraints of  $\Lambda$  and jet in different  
 336 events. For example, at one event, the azimuth phase space is separated into two sections, the  
 337 jet areas and off-axis regions, as shown in Fig.5.2. The Fig. 5.3 shows near-jet mixed events and  
 338 corresponding comparison of  $\Delta R$  distribution. If there are no constraints between  $\Lambda$  and jet at  
 339 mixed event, the  $\Lambda$  will located randomly at any region that was described above that named as  
 340 random mixed events. Therefore, it is possible for  $\Lambda$  to reconstruct a fake jet when it located at  
 341 off-axis regions where none jet exist. It means this jet was dominated by  $\Lambda$  particle, which was  
 342 verified in Fig. 5.4. This condition might affect jet  $p_T$  distribution and acceptance correction.  
 343 The Fig. 5.4 shows mixed events when  $\Lambda$  located at off-axis regions, likely to underlying event  
 344 (UE) cone. The  $\Delta R$  distribution is inconsistent with the same event.

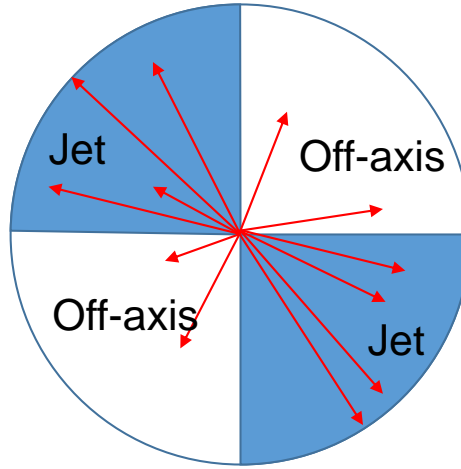


Figure 5.2: Azimuth phase space

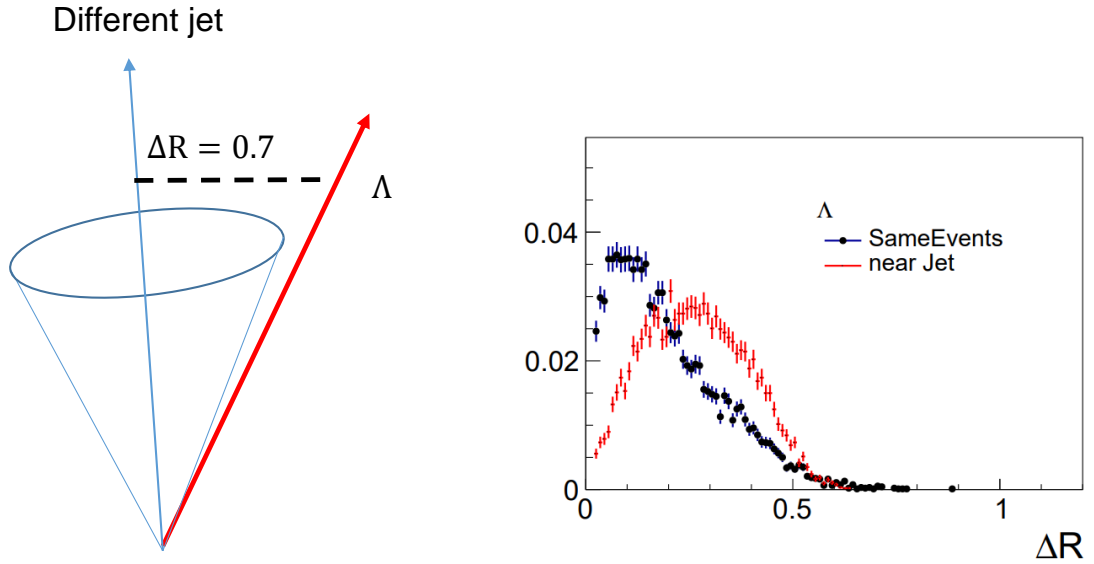


Figure 5.3: The near-jet mixed events

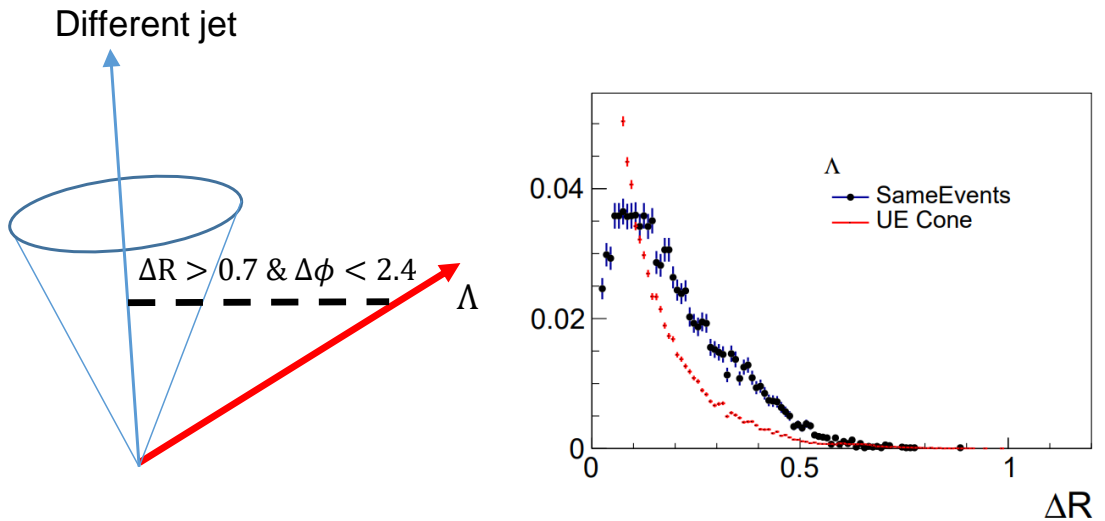


Figure 5.4: The off-jet mixed events

345 To assess the magnitude of the influence,  $\Lambda$  was required to be near the jet with  $\Delta R < 0.7$  in  
 346 mixed events prior to jet reconstruction. The quality comparison between random mixed events  
 347 and near-jet mixed events is illustrated in the following figures. There is no significant difference  
 348 in the jet  $p_T$  distribution, with the exception of the low  $p_T$  range. Removing mixed events  
 349 from the off-axis region would significantly reduce the number of fake jets with low  $p_T$  that are  
 350 predominantly composed of  $\Lambda$  particle. A positive outcome is that near-jet mixed events have  
 351 improved the consistency of the  $z$  distribution with SE. Nevertheless,  $j_T$  distribution has not  
 352 seen substantial improvement, and inconsistency persists.

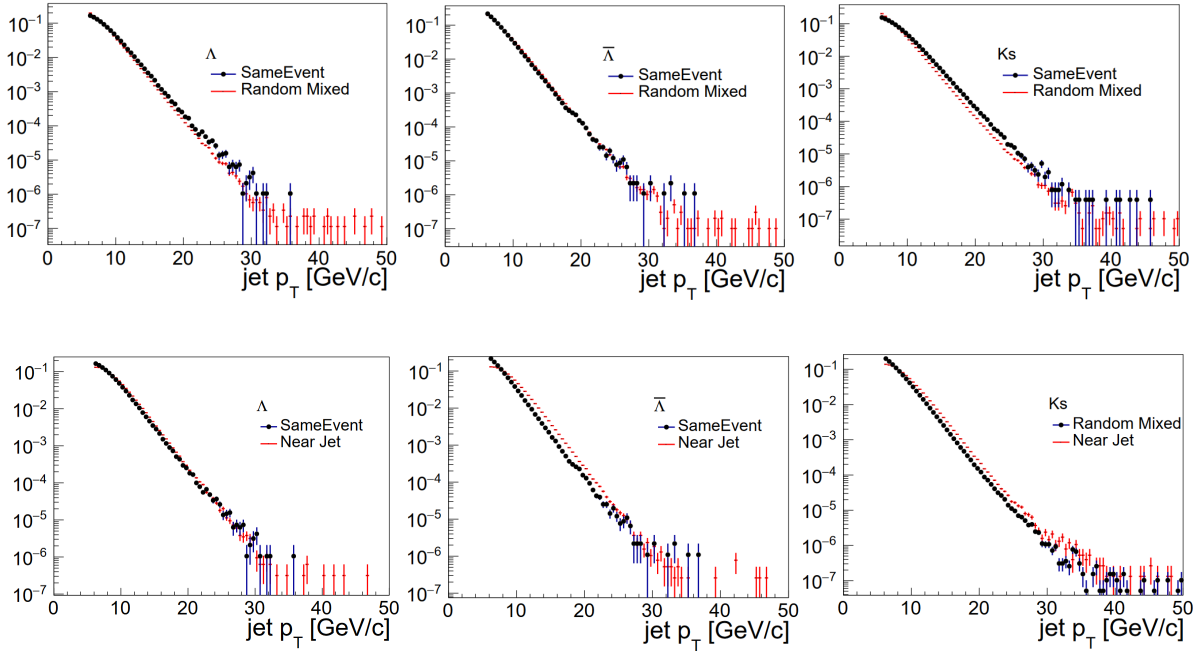


Figure 5.5: Top panel: comparisons of jet  $p_T$  between SE and random ME; Bottom panel: comparisons of jet  $p_T$  between SE and near-jet ME

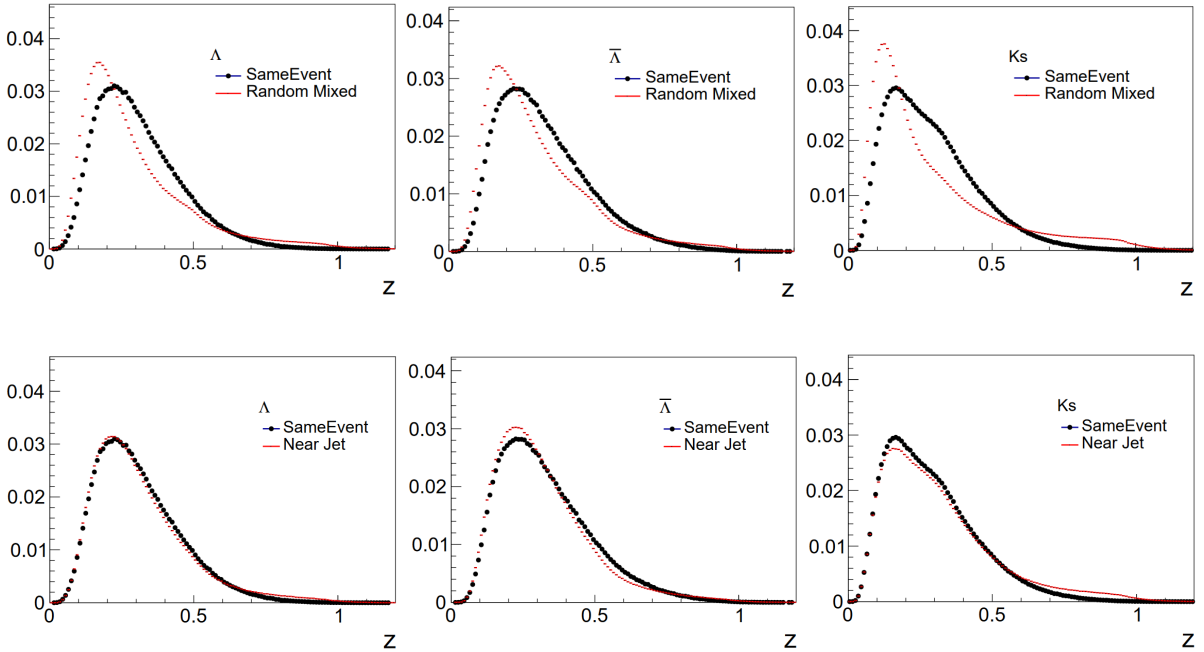


Figure 5.6: Top panel: comparisons of  $z$  between SE and random ME; Bottom panel: comparisons of  $z$  between SE and near-jet ME

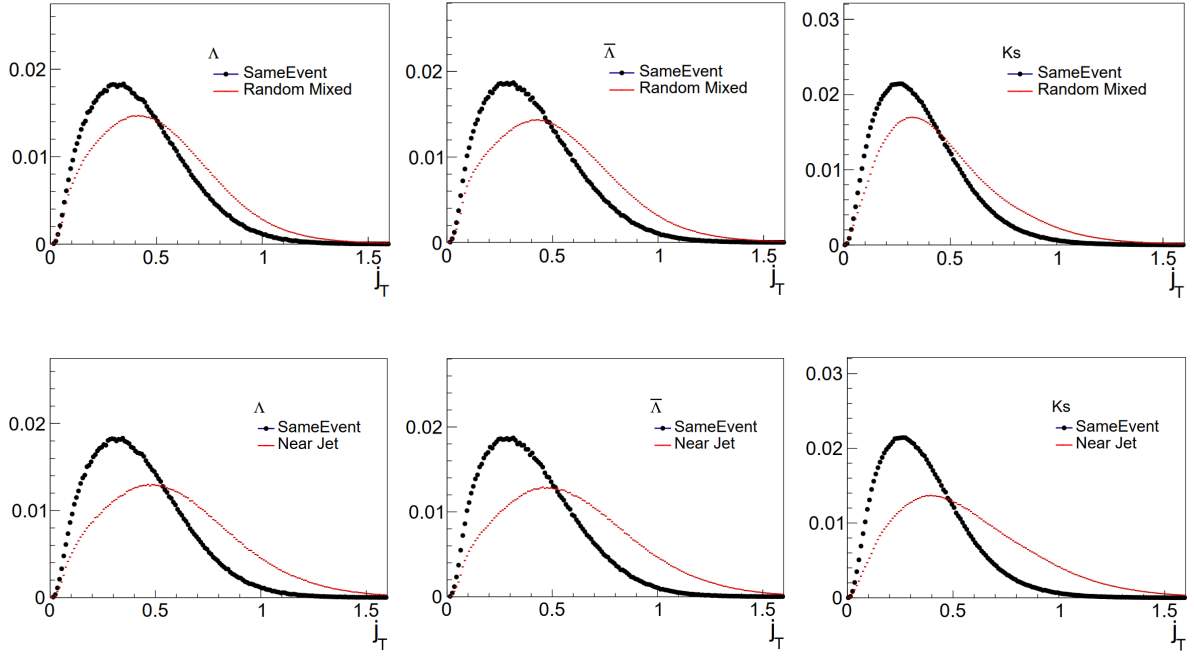


Figure 5.7: Top panel: comparisons of  $j_T$  between SE and random ME; Bottom panel: comparisons of  $j_T$  between SE and near-jet ME

353 We also compared  $\Lambda$  and  $\bar{\Lambda} \cos\theta^*$  distributions of mixed events generated by the different meth-  
 354 ods. The consistency of their distributions was very good, indicating that the off-axis region has  
 355 a minor impact on the correction of the acceptance. However, the near-jet mixed events were  
 356 closer to the true events, so we still used this method for acceptance correction in this analysis.

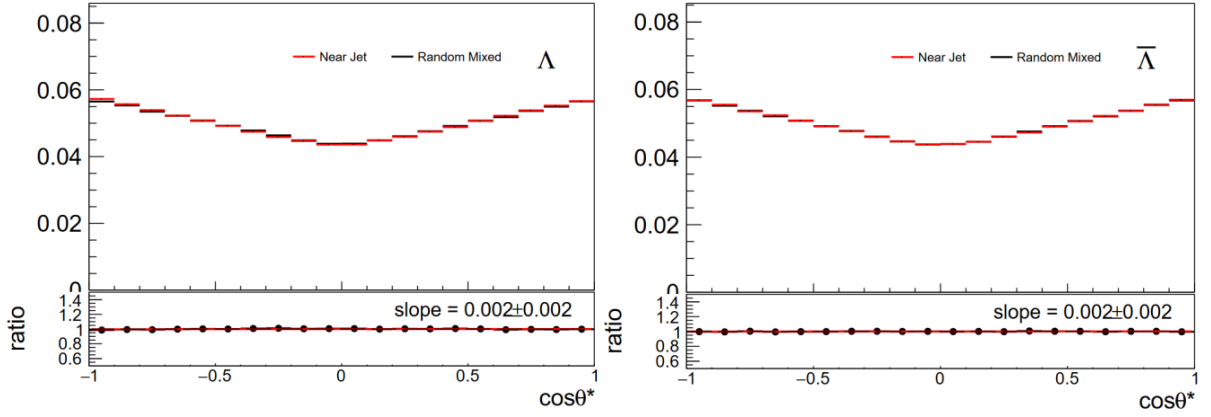


Figure 5.8: Comparison of  $\cos\theta^*$  between random and near-jet mixed event

## 357 5.2 Closure test in MC

358 The closure test for this method is unavoidable to confirm whether the mixed event method  
 359 could be useful for acceptance correction in this analysis. The following study about mixed  
 360 events is based on unpolarized MC samples, produced by Pythia6 and GEANT3 as mentioned  
 361 above. Firstly, we need to verify whether the mixed-event method will generate a non-physical  
 362 fake signals.

363 We have produced a mixed-events sample using MC simulation data. The same algorithm and  
 364 criteria of jet reconstruction are also applied in mixed-events sample. Because  $\Lambda/\bar{\Lambda}$  does not  
 365 originate from the jet in mixed events, the correlation between  $\Lambda/\bar{\Lambda}$  and the jet will differ from  
 366 that in the same event. Figure 5.9 shows the comparisons of three quantities,  $\Delta R$ ,  $z$ ,  $j_T$  that  
 367 can describe the correlation between  $\Lambda$  and jets, distributions between mixed and same events.  
 368  $\Delta R(\equiv \sqrt{(\Delta\eta)^2 + (\Delta\phi)^2})$  means the distance in  $\eta$ - $\phi$  between a hyperon and a jet. The hyperon  
 369  $z$ , the definition of which is shown in the following, denotes the longitudinal momentum fraction  
 370 of a jet carried by the hyperon. The hyperon  $j_T$  denotes the transverse momentum of  $\Lambda/\bar{\Lambda}$  w.r.t.  
 371 the jet axis.

$$z = \frac{\vec{p}_\Lambda \cdot \vec{p}_{jet}}{|\vec{p}_{jet}|^2} \quad (5.1)$$

372

$$j_T = \frac{|\vec{p}_\Lambda \times \vec{p}_{jet}|}{|\vec{p}_{jet}|} \quad (5.2)$$

373 where  $\vec{p}_\Lambda$  and the  $\vec{p}_{jet}$  are the momenta of  $\Lambda$  and jet, respectively. These three distributions  
 374 of mixed events are all inconsistent with that of the same event, which means reweighting is  
 375 necessary for mixed events.

376 These three quantities are correlated with each other from the above equations Eq. (5.1) and  
 377 Eq. (5.2). Based on our study, 2-dimensional distributions of  $\Delta R$  vs  $z$  are able to be capable  
 378 of reweighting. We will reweight 2-dimensional distributions of  $\Delta R$  vs  $z$  from mixed events,  
 379 as shown in the left of Figure 5.10, to the same events, shown in the right of Figure 5.10. The  
 380 distributions of  $\Delta R$ ,  $z$  will be consistent between the same events and mixed events as expected.  
 381 Fortunately, the hyperon  $j_T$  also becomes consistent. Figure 5.11 shows the comparisons of  $\Lambda$   
 382  $\Delta R$ ,  $z$ ,  $j_T$  between real data and mixed events after reweighting.

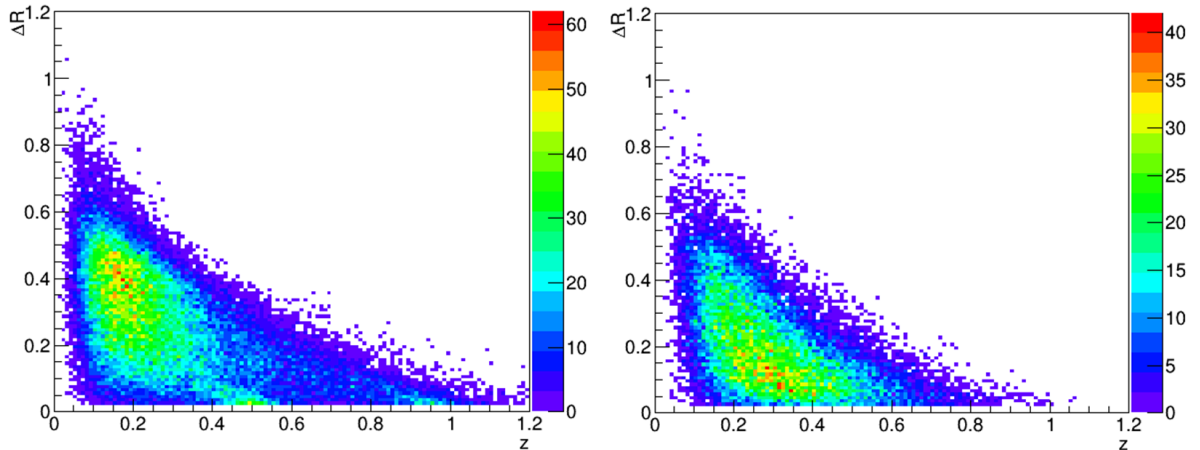
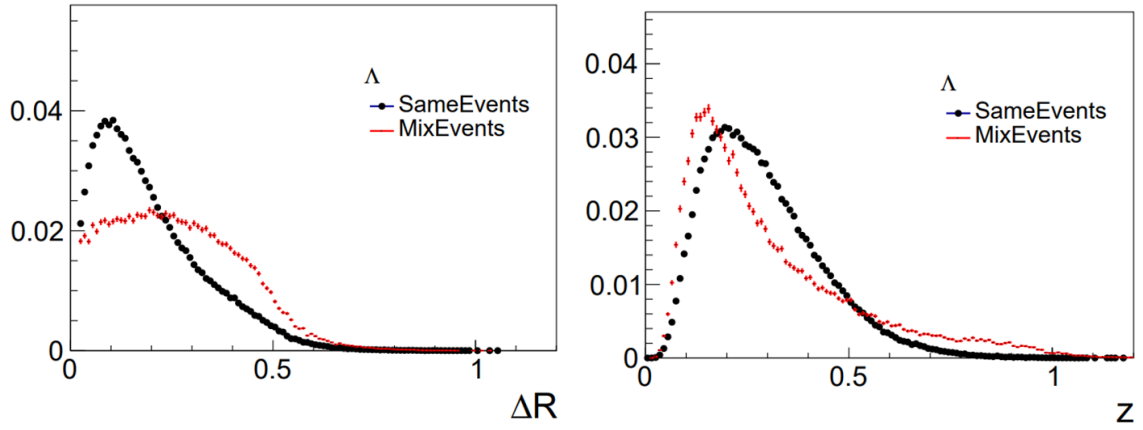
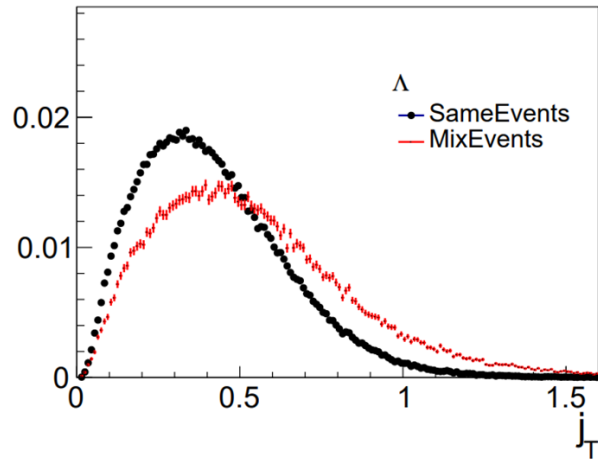


Figure 5.10: Left:  $\Delta R$  vs  $z$  of  $\Lambda$  at mixed events. Right:  $\Delta R$  vs  $z$  of  $\Lambda$  at same events



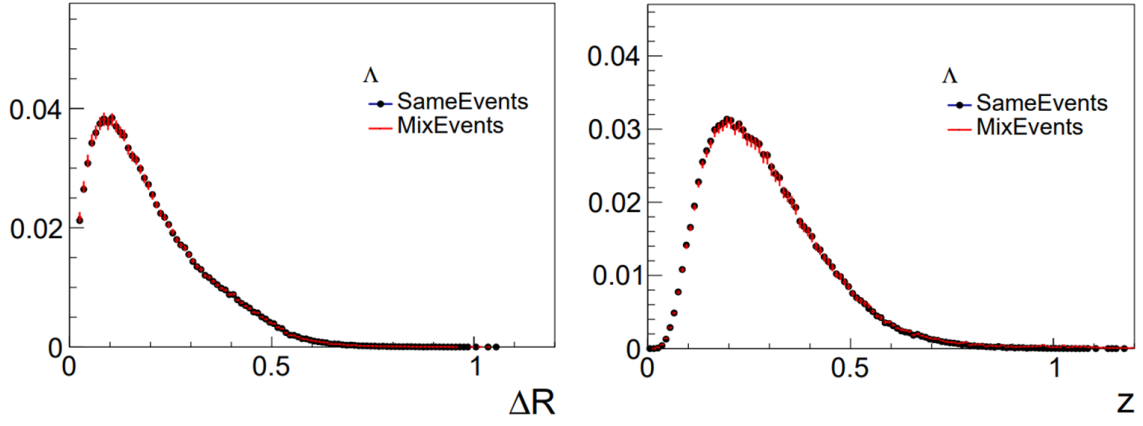
(a)  $\Delta R$  between  $\Lambda$  and jet

(b)  $\Lambda z$  distribution



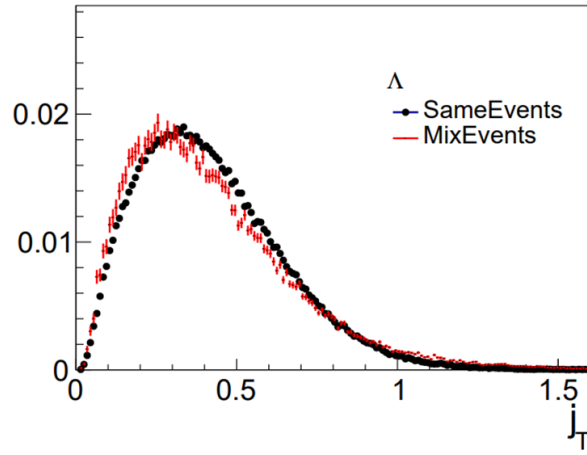
(c)  $\Lambda j_T$  distribution

Figure 5.9: Comparison of  $\Delta R, z, j_T$  distribution of  $\Lambda$  between SameEvents and MixedEvents before reweighting.



(a)  $\Delta R$  between  $\Lambda$  and jet

(b)  $\Lambda z$  distribution



(c)  $\Lambda j_T$  distribution

Figure 5.11: Comparison of  $\Delta R, z, j_T$  distribution of  $\Lambda$  between same events and mixed events after reweighting.



383 Moreover, the  $\Lambda$   $p_T$  also becomes consistent after reweighting by comparing subplots (a) and  
 384 (b) of Fig. 5.12, which means the mixed events will also change  $\Lambda$  momentum distribution and  
 385 the reweighting procedure is necessary. With regard to  $\Lambda$   $\eta$  and  $\phi$  distributions, there are no  
 large variations.

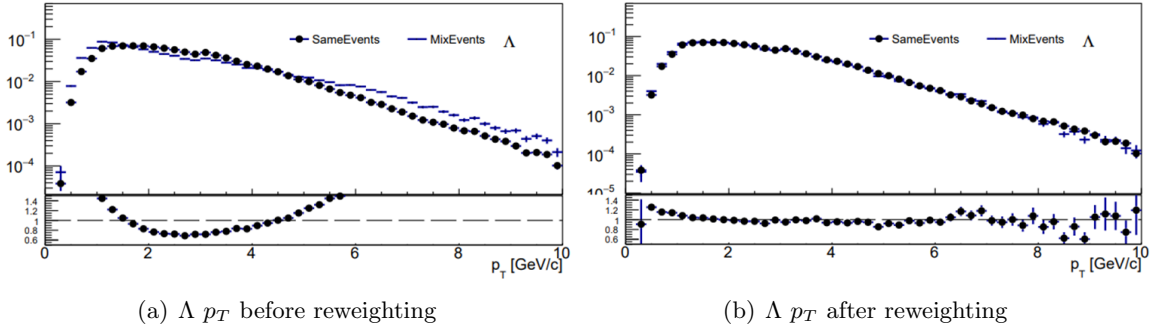


Figure 5.12: Comparison of  $\Lambda$   $p_T$  distribution between same events and mixed events.

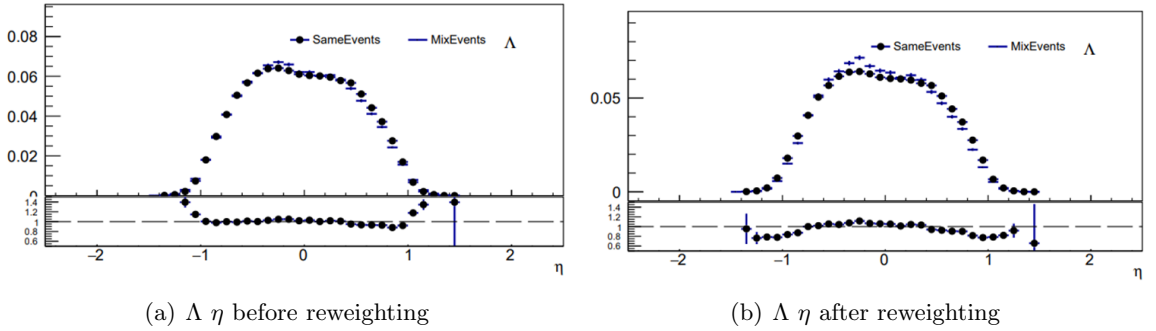


Figure 5.13: Comparison of  $\Lambda$   $\eta$  distribution between same events and mixed events.

386

387 The most important thing is whether the mixed event could describe detector acceptance effects  
 388 in our analysis. Fortunately, the behavior of  $\cos\theta^*$  with detector acceptance effects is described  
 389 well by mixed event, even though before reweighting as shown in Figure 5.15 (a). After reweight-  
 390 ing,  $\cos\theta^*$  become more consistent than before based on the slope of ratio is consistent with 0  
 391 as shown in Figure 5.15 (b), which means no extra polarization signal from the mixed event.  
 392 However, it does not mean the mixed-event method could be applied to extract polarization in  
 393 a polarized sample. We do not know how large the impacts of mixed events are for the  $\cos\theta^*$   
 394 distribution of polarized  $\Lambda$ , which is the last step of the closure test.

395 To confirm whether the mixed-event method works well in polarization extraction and how large  
 396 impacts are for the polarized  $\Lambda$  sample, we generate a MC sample with polarized  $\Lambda$  by throwing  
 397 some  $\Lambda$  randomly by a linear function of  $\cos\theta^*$ :

$$f = \alpha P_\Lambda (\cos\theta^* + 1) + 1, \quad (5.3)$$

398 where  $P_\Lambda$  is the input polarization and  $\alpha$  is the weak decay constant of  $\Lambda$ . The blue flat line in  
 399 the left plot of Fig. 5.16 is  $\cos\theta^*$  distribution with  $P_\Lambda = 0$ , and the red line is  $\cos\theta^*$  distribution  
 400 with  $P_\Lambda = -0.1$ . We fit this red line and get the same polarization signal as the input value. So

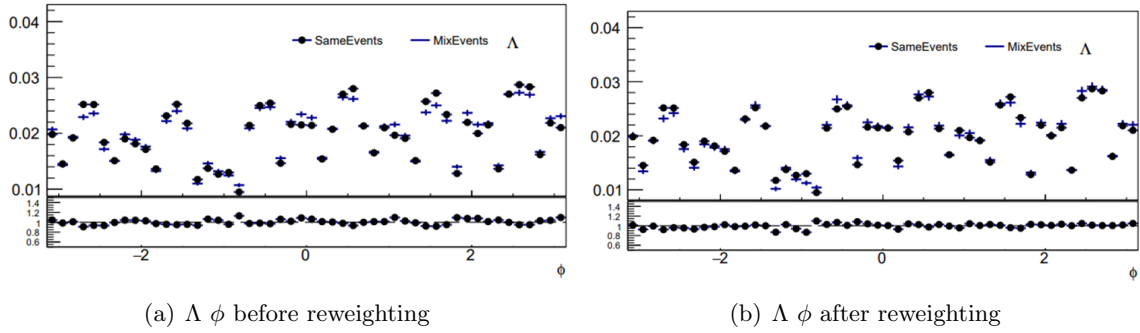


Figure 5.14: Comparison of  $\Lambda \phi$  distribution between same events and mixed events.

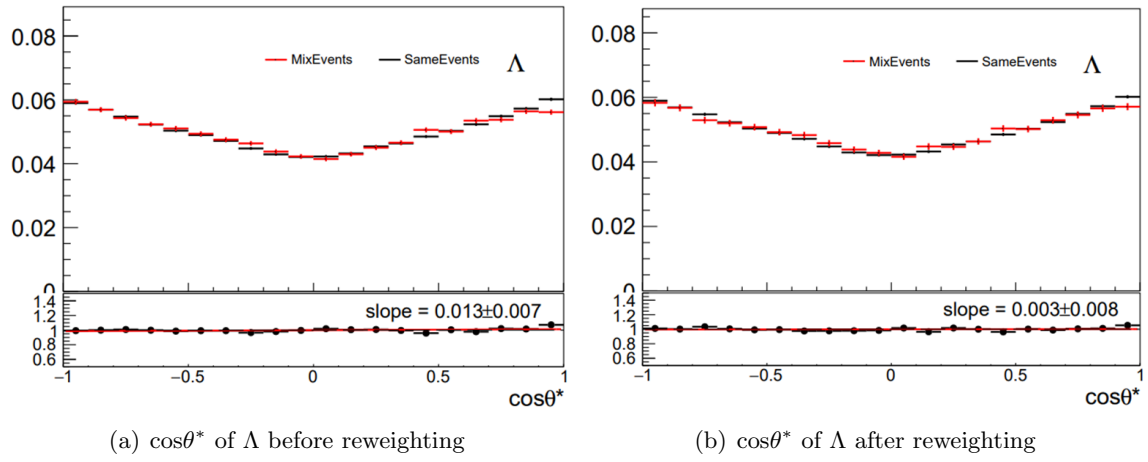


Figure 5.15: Comparison of  $\cos\theta^*$  of  $\Lambda$  between same events and mixed events.

401 we used the same method at the detector level. Then, we use this polarized lambda sample to  
 402 make the mixed event.

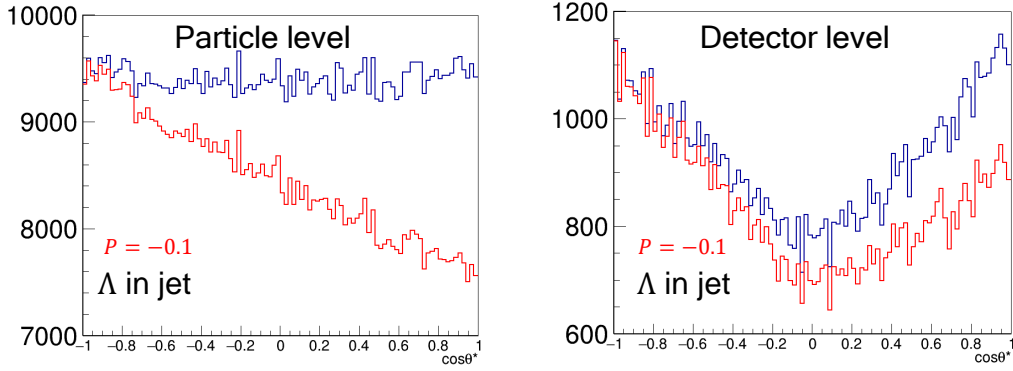


Figure 5.16: Left:  $\cos\theta^*$  of  $\Lambda$  at particle level. Right:  $\cos\theta^*$  of  $\Lambda$  at detector level

403 The results with different input polarization are shown in Fig. 5.17. The y-axis denotes extracted  
 404 polarization, and the x-axis is input polarization. The red dashed line is a reference axis with the  
 405 function  $y=x$ . As we can see, the extracted polarizations are consistent with input polarizations.  
 406 Therefore, the mixed event method is reliable in the polarization extraction.

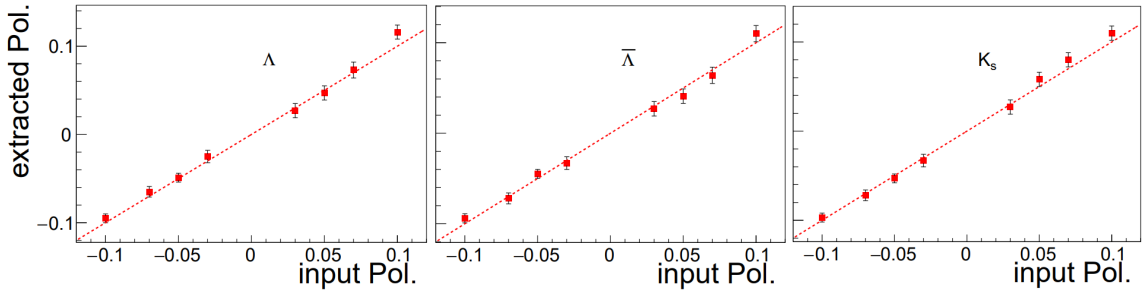


Figure 5.17: Extracted polarization vs input polarization of  $\Lambda$ ,  $\bar{\Lambda}$  and  $K_s^0$

Closure test				
Input polarization	-0.1	-0.07	-0.05	-0.03
Extracted $P_\Lambda$	$-0.095 \pm 0.005$	$-0.065 \pm 0.006$	$-0.049 \pm 0.005$	$-0.025 \pm 0.007$
Extracted $P_{\bar{\Lambda}}$	$-0.094 \pm 0.005$	$-0.072 \pm 0.006$	$-0.045 \pm 0.005$	$-0.033 \pm 0.007$
Extracted $P_K$	$-0.097 \pm 0.005$	$-0.072 \pm 0.006$	$-0.053 \pm 0.005$	$-0.033 \pm 0.007$
Input polarization	0.03	0.05	0.07	0.10
Extracted $P_\Lambda$	$0.027 \pm 0.008$	$0.047 \pm 0.008$	$0.073 \pm 0.009$	$0.116 \pm 0.008$
Extracted $P_{\bar{\Lambda}}$	$0.027 \pm 0.008$	$0.041 \pm 0.008$	$0.064 \pm 0.009$	$0.11 \pm 0.009$
Extracted $P_K$	$0.027 \pm 0.008$	$0.058 \pm 0.008$	$0.08 \pm 0.008$	$0.11 \pm 0.008$

Table 5.1: The table of  $\Lambda$  extracted polarization and input polarization

### 407 5.3 Mixed-events sample

408 A thorough quality assessment (QA) of the mixed-event sample is crucial before applying accep-  
 409 tance corrections. As noted above, this involves comparing the distributions of several quantities  
 410 between the mixed events and the corresponding single events. Meanwhile, it was observed that  
 411 discrepancies in the  $\Delta\eta$  vs  $\eta_{jet}$  distribution might impact acceptance correction, even after 3-  
 412 dimensional reweighting in  $\Delta R, z, p_T^{jet}$ .  $\Delta\eta$  here was defined as  $\Delta\eta = \eta_H - \eta_{jet}$ . Figure 5.18  
 413 displays a 2D distribution of  $\Delta\eta$  vs  $\eta_{jet}$  distributions for  $K_s^0$  in both mixed events and same  
 414 event. A clear asymmetry in  $\Delta\eta$  was observed at opposite  $\eta_{jet}$  regions in the mixed events,  
 415 inconsistent with the same event distribution. In order to remove potential effects on the accep-  
 416 tance correction, a 2D reweighting of  $\Delta\eta$  vs  $\eta_{jet}$  was implemented in addition to the existing  
 417 3-dimensional reweighting of  $\Delta R, z, p_T^{jet}$ .

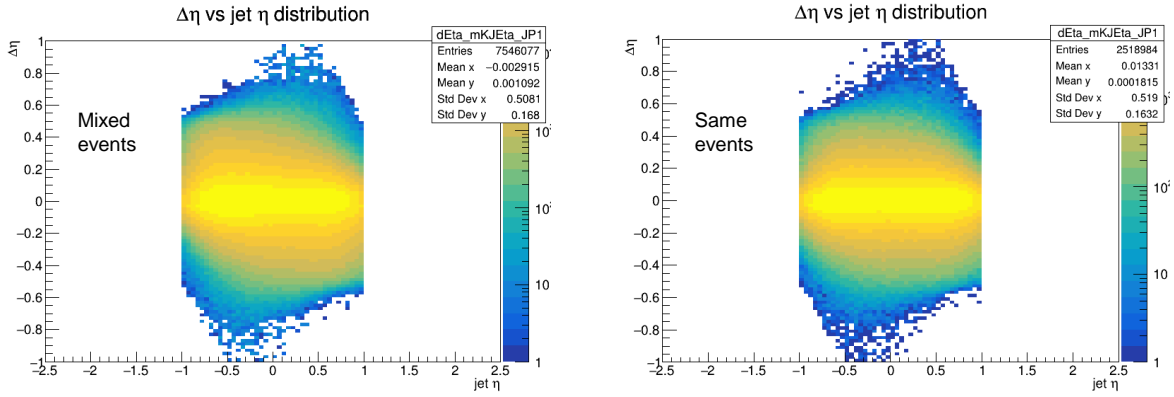


Figure 5.18: Left:  $\Delta\eta$  vs  $\eta_{jet}$  in mixed events. Right:  $\Delta\eta$  vs  $\eta_{jet}$  in same events.

418 The kinematic consistencies, such as transverse momentum ( $p_T$ ), pseudorapidity ( $\eta$ ), and az-  
 419 imuthal angle ( $\phi$ ), are well-maintained after the reweighting process. Furthermore, the com-  
 420 parison of certain correlated quantities between hyperons and jets post-reweighting is presented  
 421 below. The results demonstrate satisfactory consistencies for these quantities, indicating that  
 422 the mixed events sample is capable of effectively performing acceptance corrections.

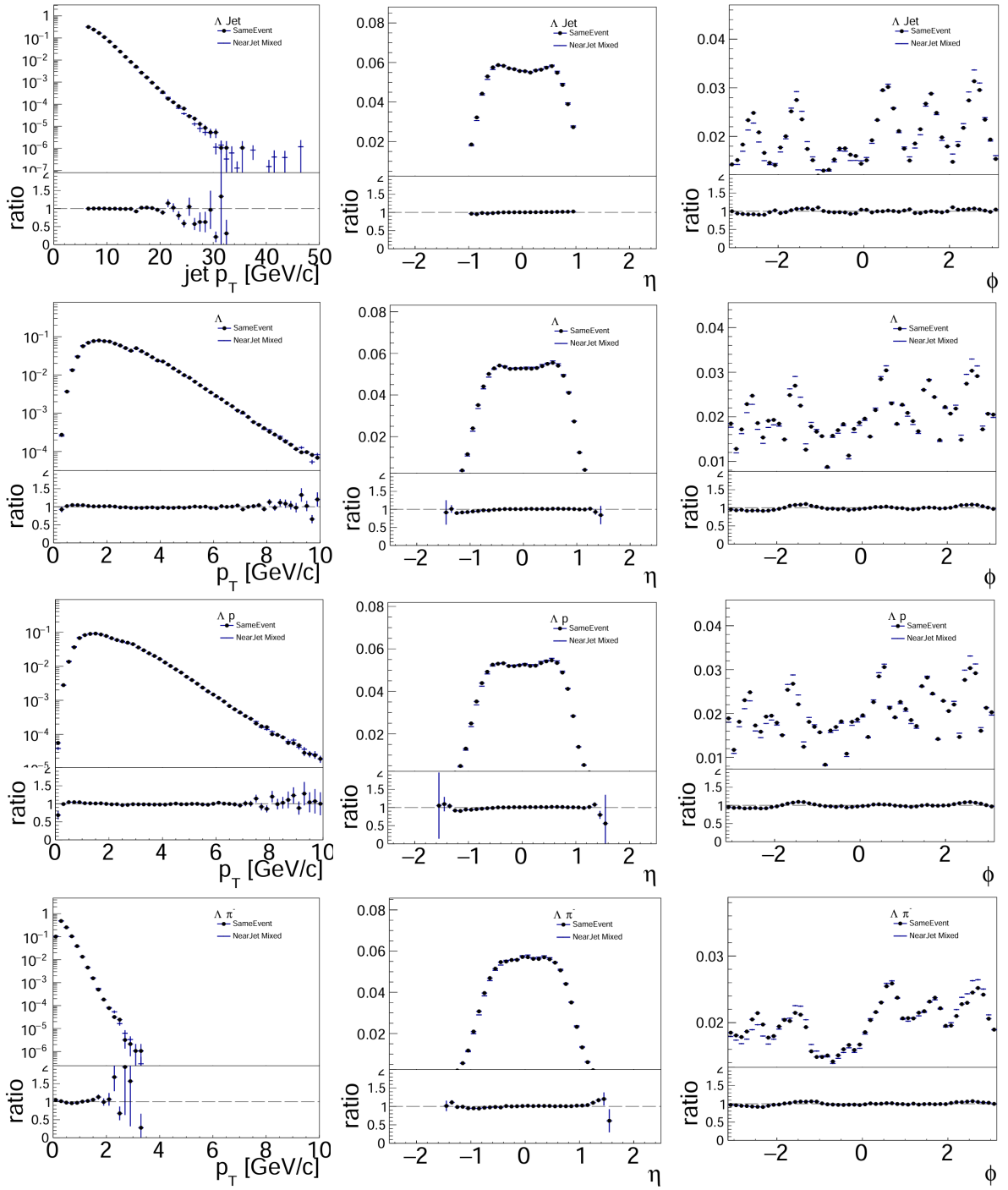


Figure 5.19: Comparisons of three kinematic quantities  $p_T, \eta, \phi$  of  $\Lambda$  and jet between SE and ME.

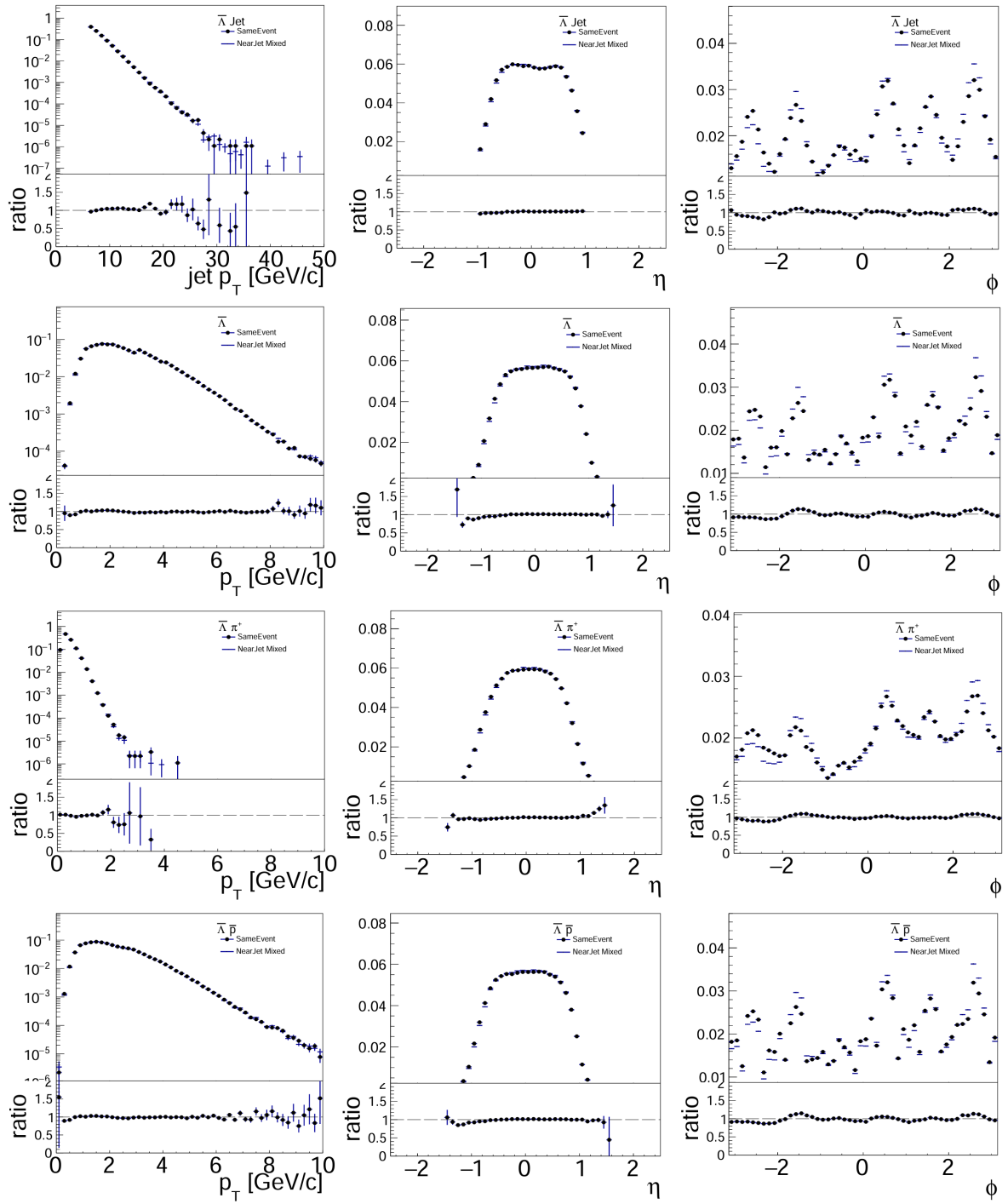


Figure 5.20: Comparisons of three kinematic quantities  $p_T, \eta, \phi$  of  $\bar{\Lambda}$  and jet between SE and ME.

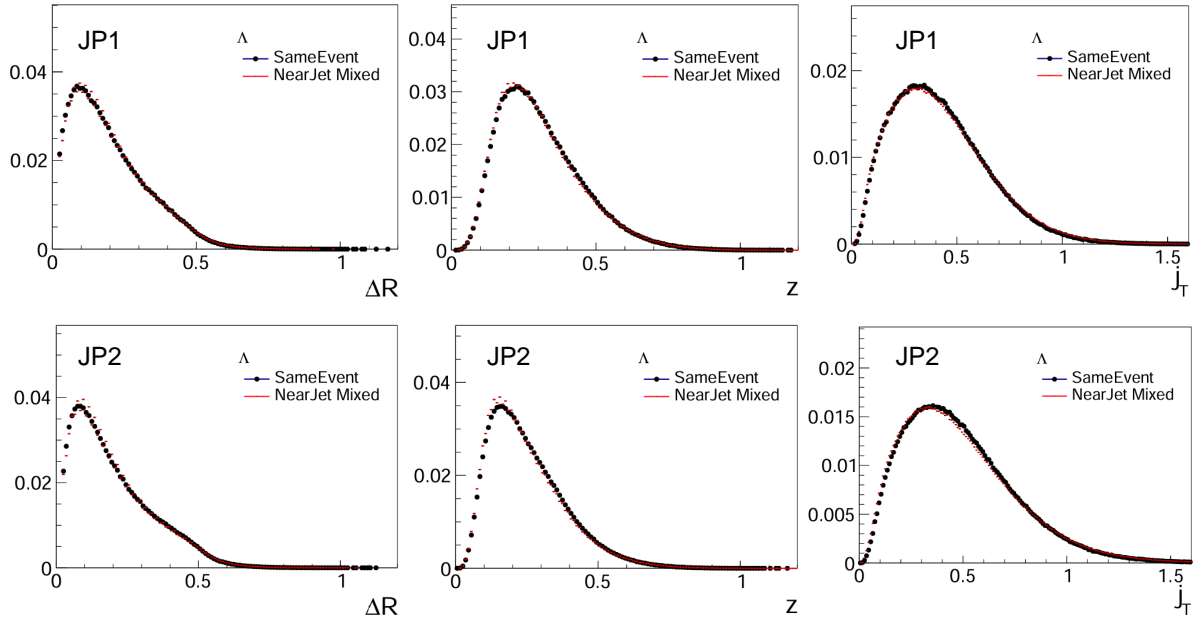


Figure 5.21: Comparisons of  $\Delta R, z, j_T$  of  $\Lambda$  between SE and ME.

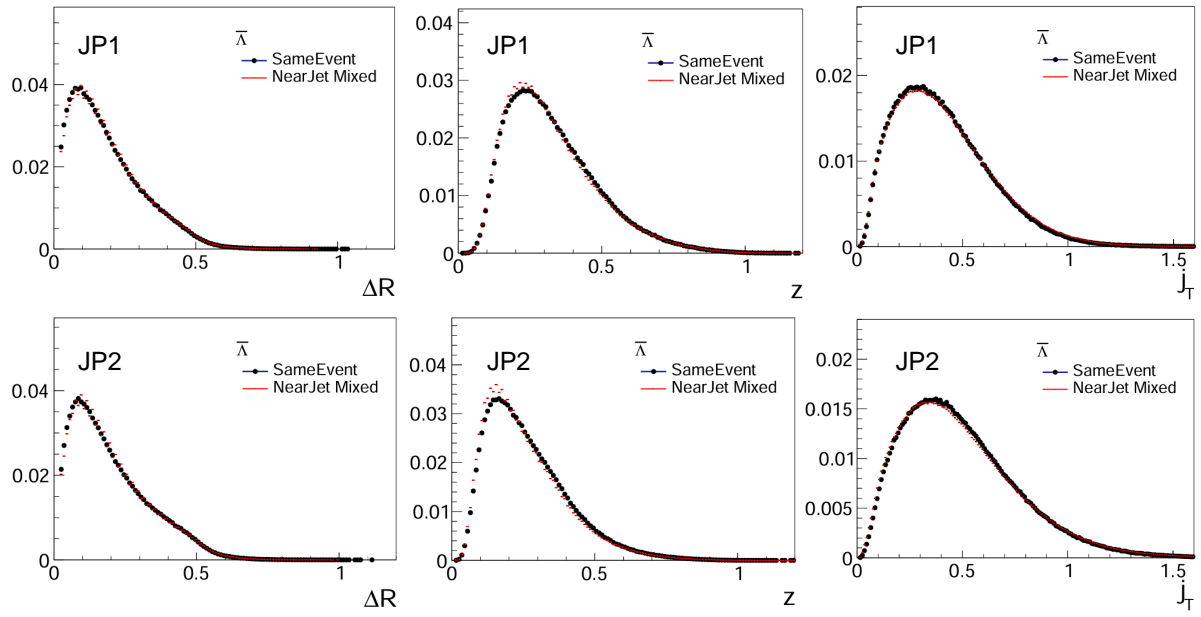


Figure 5.22: Comparisons of  $\Delta R, z, j_T$  of  $\bar{\Lambda}$  between SE and ME.

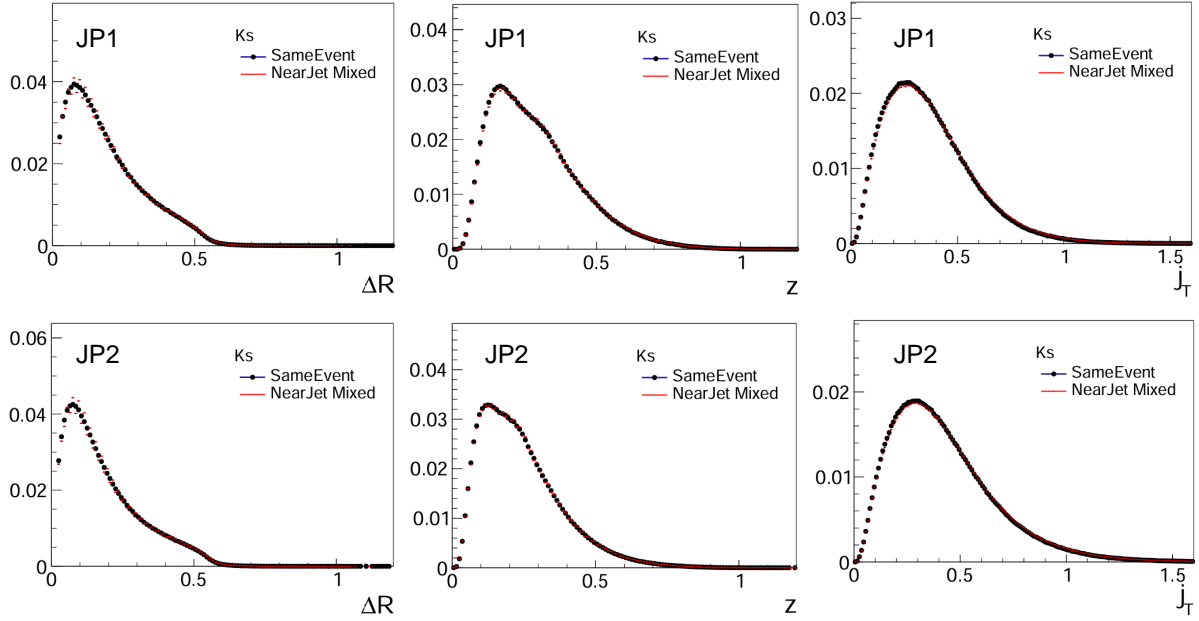


Figure 5.23: Comparisons of  $\Delta R, z, j_T$  of  $K_s^0$  between SE and ME.

## 423 6 Transverse polarization $P_{\Lambda/\bar{\Lambda}}$ extraction of $\Lambda/\bar{\Lambda}$

### 424 6.1 Detector acceptance correction

425 Here shows the procedure of acceptance correction and lambda polarization extraction. The  
 426  $\cos\theta^*$  distribution of  $\Lambda$  is not linear, as shown in Figure 6.1, which is attributed to the detector  
 427 acceptance effects. Here, the mass peak window of the candidates  $\Lambda$  is set at  $1.112 \sim 1.120$   
 428 GeV/c and background contribution had been subtracted from the  $\cos\theta^*$  distribution under the  
 429 mass peak using the sideband method, as shown in Figure 2.2.

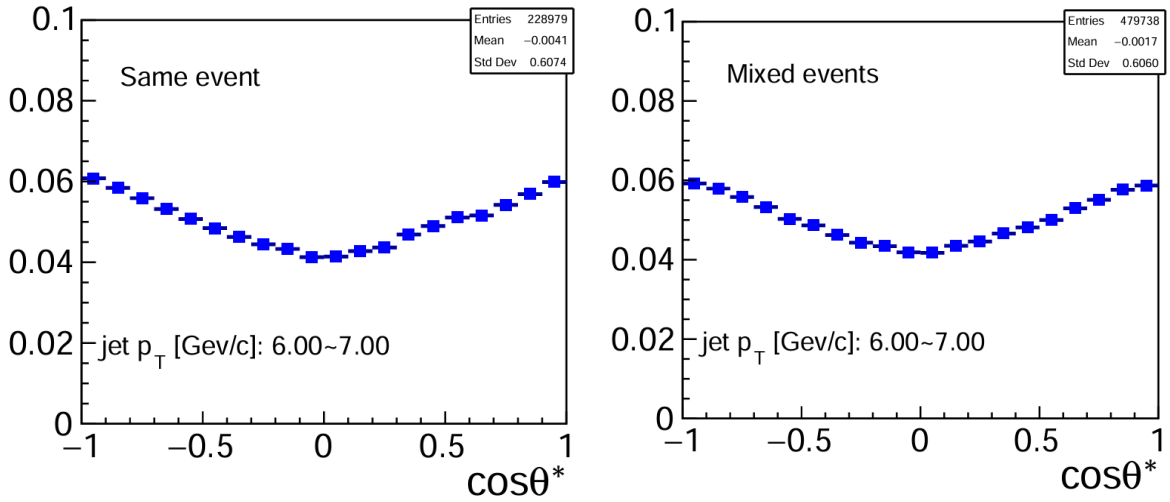


Figure 6.1:  $\cos\theta^*$  distribution of  $\Lambda$  for the same event(left) and mixed events(right)



430 The acceptance correction can be done via mixed events. The  $\cos\theta^*$  distribution of  $\Lambda$  that could  
 431 reflect detector acceptance can be seen in the right panel of Figure 6.1. The same background  
 432 subtraction procedure was also applied for mixed events. Once the acceptance correction is  
 433 done, polarization can be extracted by fitting the  $\cos\theta^*$  distribution with a linear function:

$$dN/d(\cos\theta^*) = A(\cos\theta^*)(1 + \alpha P_\Lambda \cos\theta^*) \quad (6.1)$$

434 where  $A(\cos\theta^*)$  denotes acceptance function. The  $\alpha$  is the weak decay constant of  $\Lambda$ , which is  
 435  $\alpha = 0.747 \pm 0.009$  [9]. The magnitude of weak decay constant for  $\bar{\Lambda}$  is  $\alpha = 0.757 \pm 0.004$ .

436 Figure 6.2, as an example, shows the  $\cos\theta^*$  distribution of  $\Lambda$  after acceptance correction, and it  
 437 was fitted by above function Eq.(6.1) to obtain polarization. The first fitting parameter  $p_0$  is  
 438 the extracted polarization. Its uncertainty from the fitting is treated as statistical uncertainty.  
 439 Figure 6.3 and 6.4 show the fitting results at each jet bin for  $\Lambda$  and  $\bar{\Lambda}$  respectively.

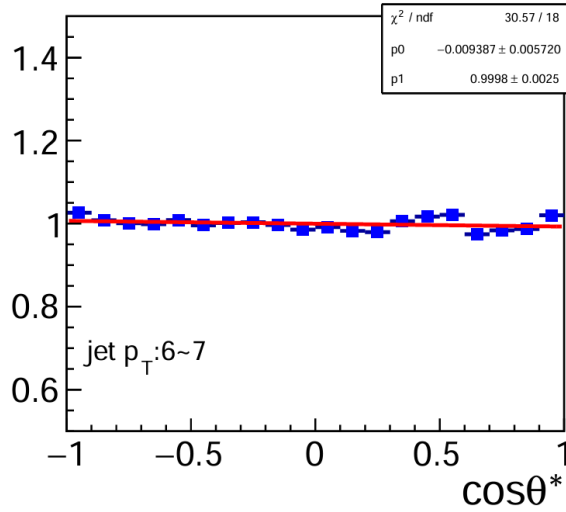


Figure 6.2:  $\cos\theta^*$  distribution of  $\Lambda$  after acceptance correction and was fitted with a linear function (red line) to extract polarization

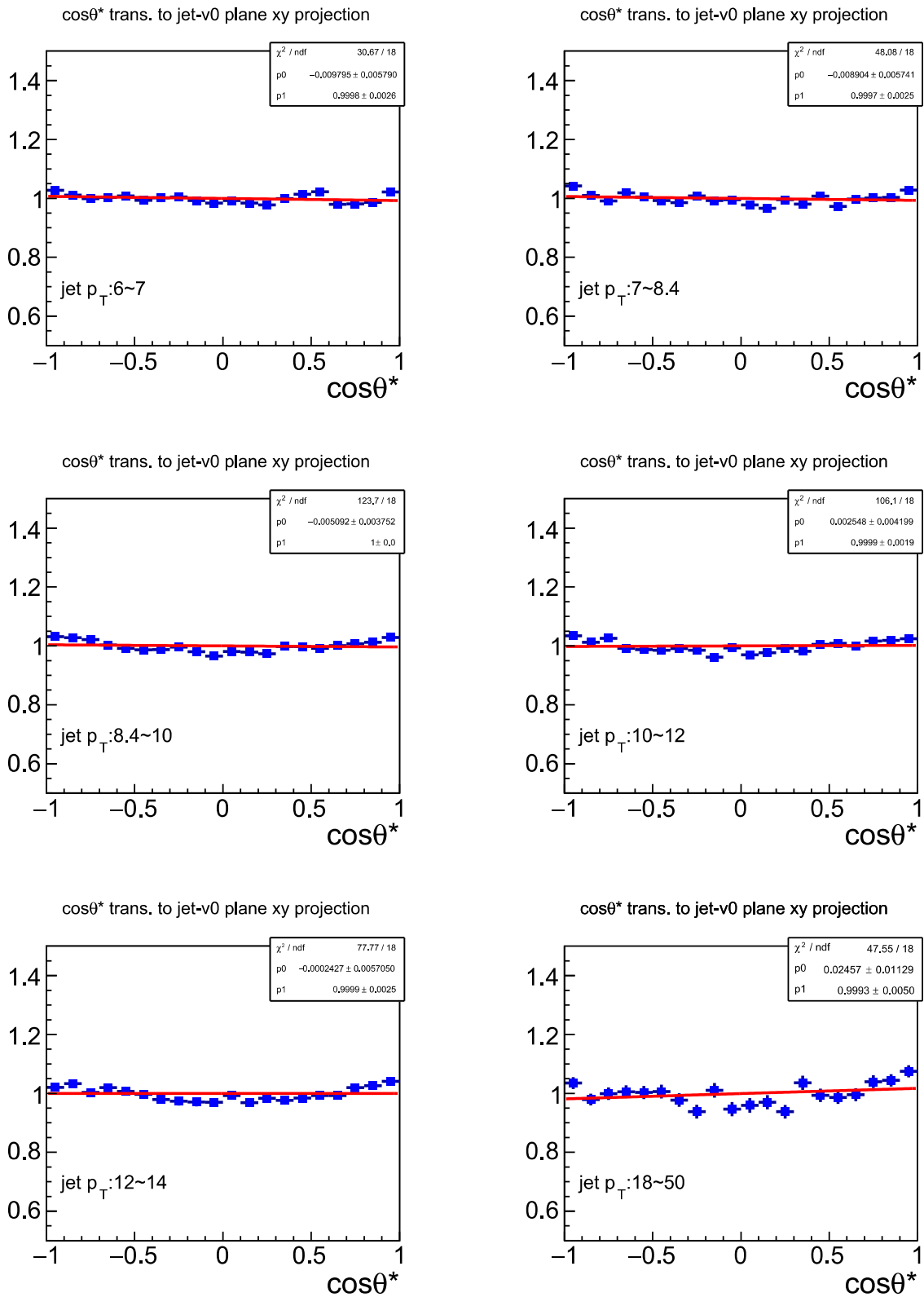


Figure 6.3: Extraction of transverse polarization of  $\Lambda$  as a function of jet  $p_T$

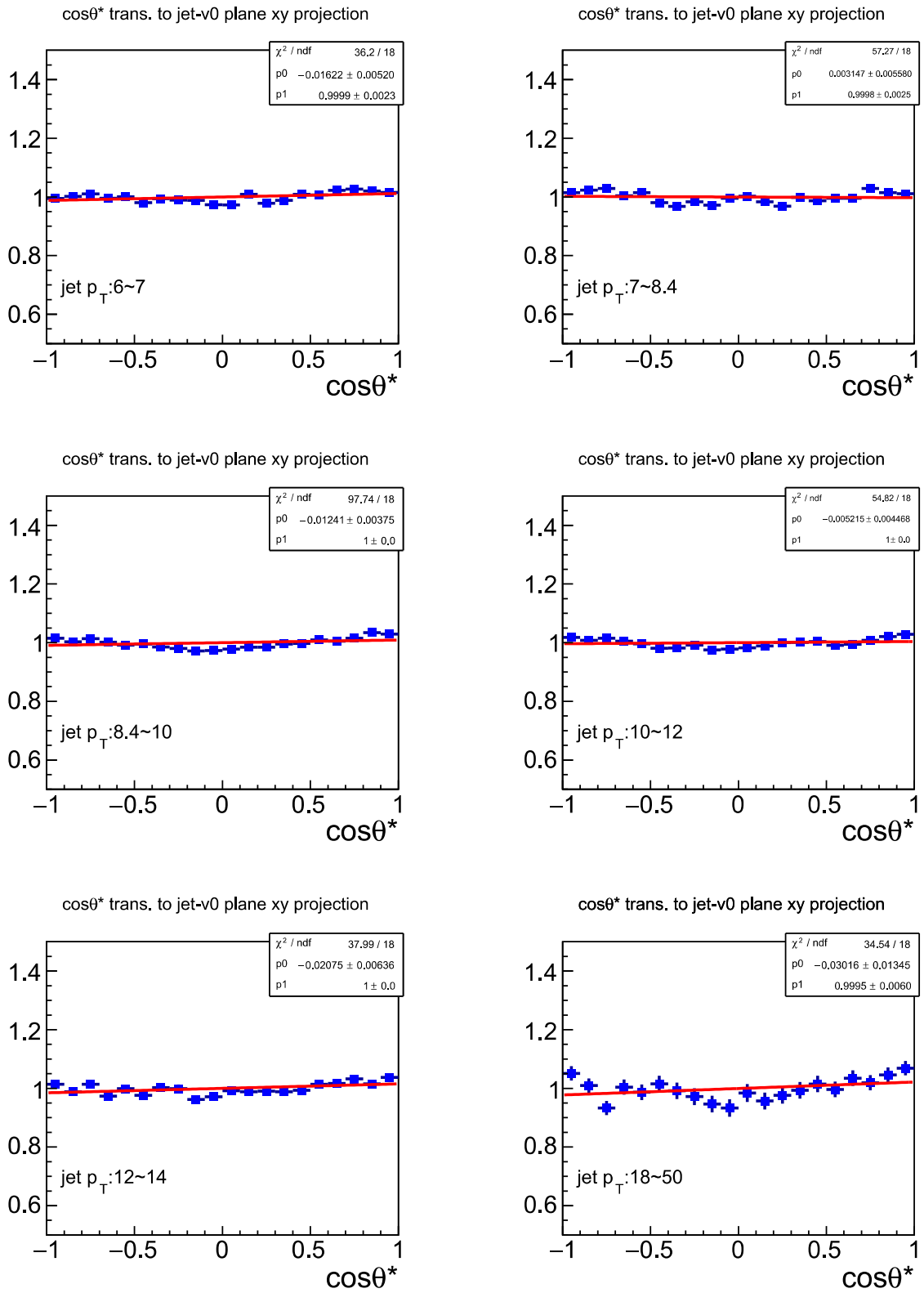


Figure 6.4: Extraction of transverse polarization of  $\bar{\Lambda}$  as a function of jet  $p_T$

440 **6.2 Zero-test with  $K_s^0$**

441 In order to confirm the validity of polarization extraction of  $\Lambda$  and  $\bar{\Lambda}$ , the  $K_s^0$  particle with  
 442 zero spin is used to make zero-test. If extracted polarizations of  $K_s^0$  are consistent with 0, it  
 443 means the  $\Lambda$  and  $\bar{\Lambda}$  polarizations extracted in this analysis are credible. The same procedure  
 444 of polarization extraction is applied for  $K_s^0$  particle. The transverse polarization of  $K_s^0$  as a  
 445 function of jet  $p_T$  is consistent with 0 as shown in Figure 6.5.

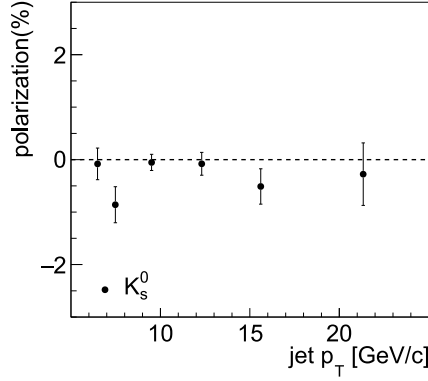


Figure 6.5: Transverse polarization of  $K_s^0$  as a function of jet  $p_T$

446 Besides, figure 6.6 and 6.7 present the transverse polarization of  $K_s^0$  as a function of  $z$  and  $j_T$ .  
 447 They are all consistent with 0 as expected, which means the method of polarization extraction  
 448 in this analysis is credible.

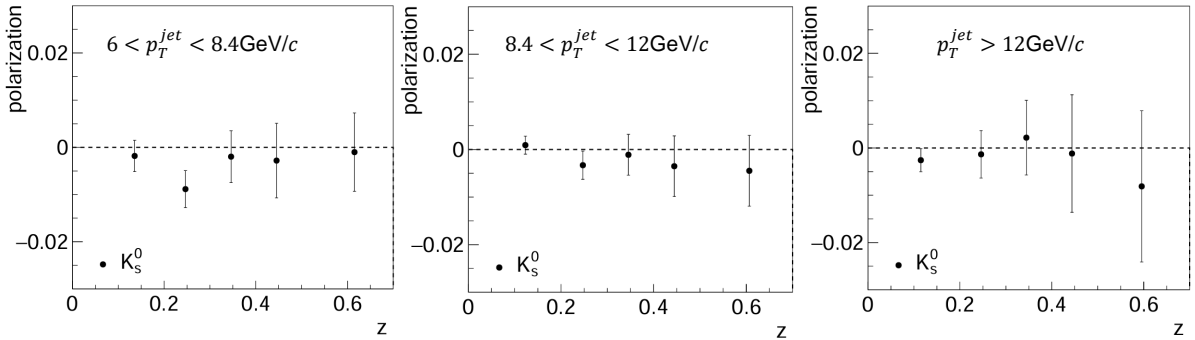


Figure 6.6: Transverse polarization of  $K_s^0$  as a function of  $z$  at different jet  $p_T$  ranges

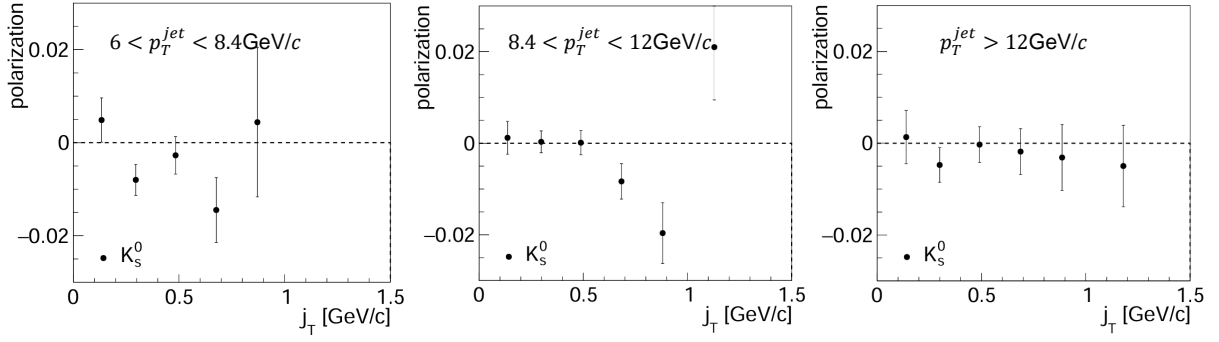


Figure 6.7: Transverse polarization of  $K_s^0$  as a function of  $j_T$  at different jet  $p_T$  ranges

### 449 6.3 Comparison of results extracted by mixed events and MC

450 We also make a cross-check by comparing the results extracted by two different methods. The  
 451 results are consistent with each other.

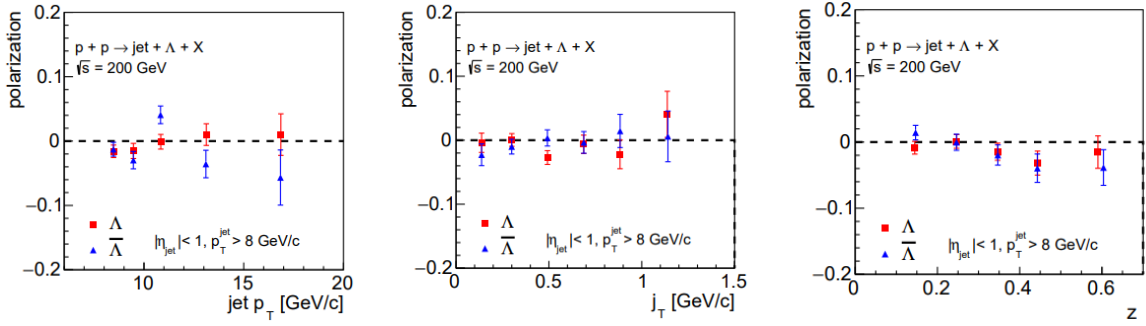


Figure 6.8: Transverse polarization extracted by MC

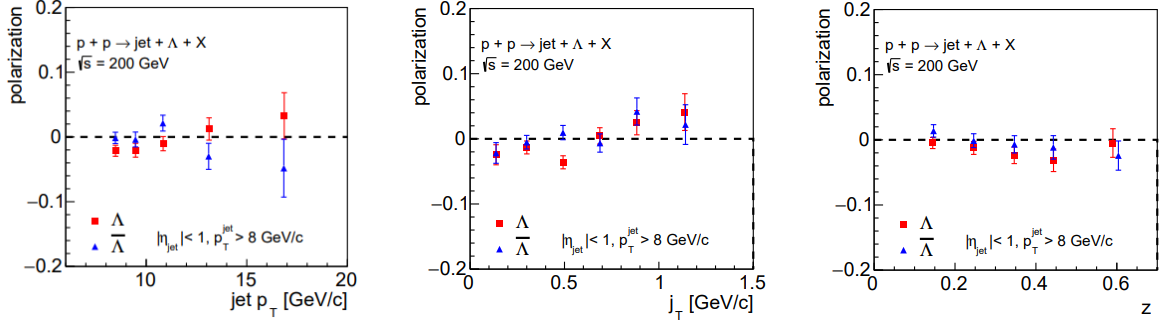


Figure 6.9: Transverse polarization extracted by mixed events

## 452 7 Systematic uncertainties

453 Four sources of systematic uncertainties are taken into account. The first one is resulted from  
 454 trigger effects, which will impact jet flavor and transverse momentum. The next systematic  
 455 uncertainty originates from the variation of side-band range for background subtraction. The

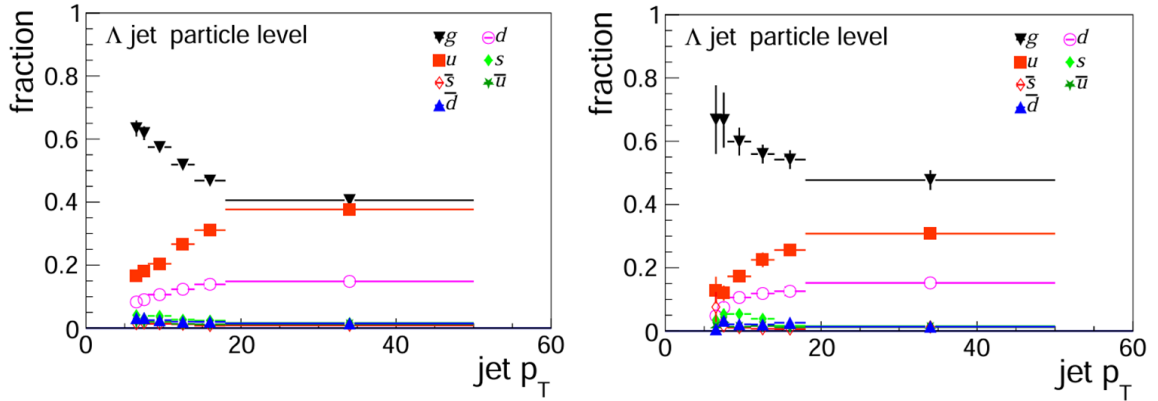
456 precision of decay parameter of  $\Lambda$  and  $\bar{\Lambda}$  also contribute to the systematic uncertainties. The  
 457 last one is contributed from the mixed event method.

## 458 7.1 Trigger Bias

459 In the data taking of STAR, trigger sets will impact jet transverse momentum and flavor fraction,  
 460 especially at the edge of trigger threshold. This effect was simulated using embedding sample  
 461 to estimate how large variation of jet flavor resulted by it. The two flavor fraction distributions  
 462 at different jet  $p_T$  are presented at Fig. 7.1. The left plot is for no-bias sample and right one is  
 463 for triggered sample. By comparing these two distributions from Fig. 7.1, the variation of quark  
 464 fraction are used to estimate the systematic uncertainty with the following formula:

$$\sigma_{\text{trig}} = \left| \frac{f_{\text{nobias}} - f_{\text{trigger}}}{f_{\text{nobias}}} \right| \times \max(P_{\Lambda}, \sigma_{\text{stat}}), \quad (7.1)$$

465 where  $f_{\text{nobias}}$  and  $f_{\text{trigger}}$  are the sum of all quark fraction of no-bias sample and trigger-bias  
 466 sample, respectively. Here,  $P_{\Lambda}$  is measured  $\Lambda$  polarization and  $\sigma_{\text{stat}}$  is statistical error of  $\Lambda$   
 467 polarization. In case  $\sigma_{\text{trig}}$  is too small as the measured  $\Lambda$  polarization is closed to zero, the  
 468 maximum of  $P_{\Lambda}$  and  $\sigma_{\text{stat}}$  is applied to calculation.



(a) Flavor fraction distribution without no-bias sam- (b) Flavor fraction distribution with triggered sample  
 ple

Figure 7.1: Flavor fraction distribution of  $\Lambda$  at different jet  $p_T$ .

## 469 7.2 Mixed event method

470 The second source comes from the ME correction in correcting the detector acceptance. A  
 471 closure test is performed with the MC sample by manually putting a polarization signal into  
 472 the generator level and then extract the polarization at detector level using the ME method.  
 473 The extracted results are consistent with input value as shown before. The following figure 7.2  
 474 shows the relative difference between them. We fitted 6 points from -0.07 to 0.07, which is close  
 475 to the range of our polarization results, and obtain mean value of the relative differences up to  
 476  $3\% \pm 5\%$ . The higher value 5% as a scale uncertainty is taken as systematic uncertainty.

## 477 7.3 Background estimation

478 The side-band method was applied to make background estimation and subtraction, as shown  
 479 in Fig. 2.2. The background  $dN/d(\cos\theta)$  distribution is subtracted from  $dN/d(\cos\theta)$  distribution

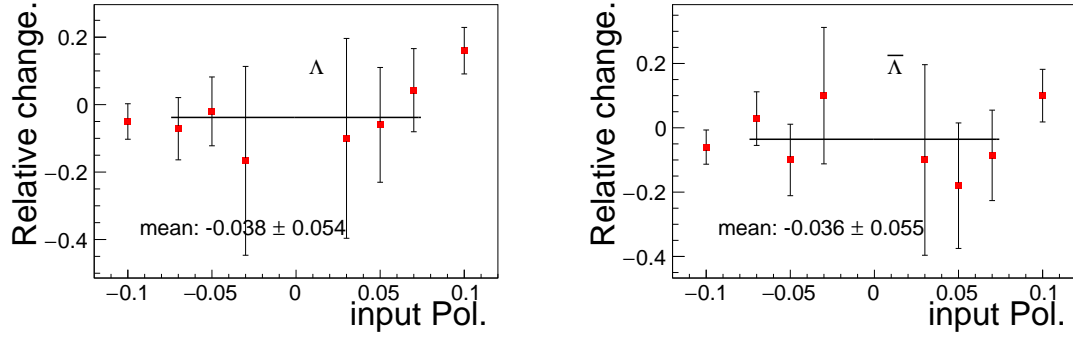


Figure 7.2: Relative change between inputted and extracted polarization.

480 under  $\Lambda$  peak range. The estimated background varies with different choices of side-band re-  
 481 gion. Therefore, the choice of side-band will introduce a potential uncertainty to the measured  
 482 polarization. This uncertainty is estimated by varying the side-band region. The polarizations  
 483 are calculated with the varied side-band region and the maximum of change of  $P_\Lambda$  resulted by  
 484 variation of side-band window are treated as the systematic uncertainties.

$$\sigma_{\text{bkg}} = \Delta P_\Lambda = |\max(P_\Lambda - P_{\text{bkg}})| \quad (7.2)$$

485 where  $P_{\text{bkg}}$  is the extracted  $\Lambda$  polarization under varied side-band shift. And  $\sigma_{\text{bkg}}$  denotes  
 486 background systematic uncertainty.

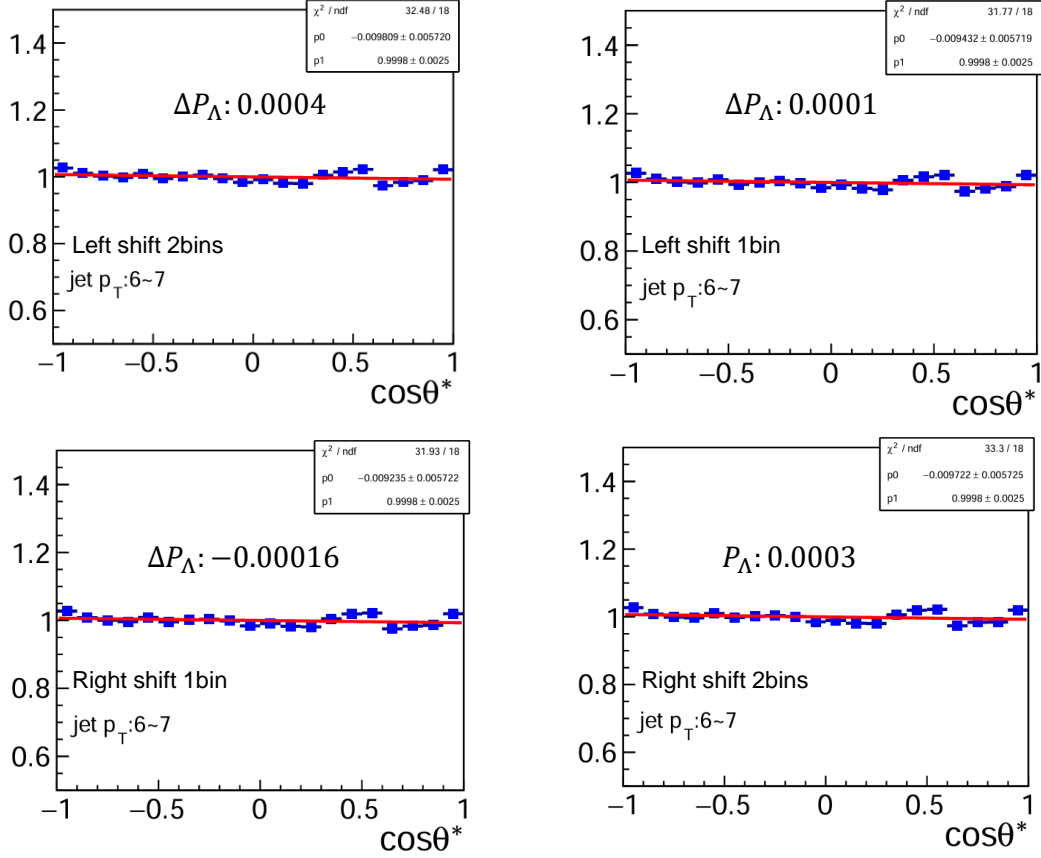


Figure 7.3: The extracted  $\Lambda$  polarization under varied side-band shift. The top two panels show polarization extraction under left shift of side-band, the bottom two panels show the polarization extraction under right shift of side-band.

#### 487 7.4 Decay parameter

488 The last source of systematic uncertainties is from the precision of weak decay constants of  $\Lambda$  and  
 489  $\bar{\Lambda}$ . In this analysis, the weak decay constant  $\alpha$  of  $\Lambda$  and  $\bar{\Lambda}$  are:  $0.747 \pm 0.009$  and  $-0.757 \pm 0.004$   
 490 respectively [9]. The systematic uncertainties from decay parameter relative to  $P_\Lambda$  is calculated  
 491 by the following equation:

$$\sigma_\alpha = 0.009/0.747 \times |P_\Lambda| \quad (7.3)$$

492 The total systematic uncertainty  $\sigma_{\text{sys}}$  is calculated through following formula:

$$\sigma_{\text{sys}} = \sqrt{\sigma_{\text{trig}}^2 + \sigma_{\text{bkg}}^2 + \sigma_\alpha^2 + \sigma_{\text{mix}}^2} \quad (7.4)$$

493 The systematic uncertainties  $\sigma_{\text{sys}}$  at different jet  $p_T$  range for  $\Lambda$  and  $\bar{\Lambda}$  are summarized in Table  
 494 7.1 and 7.2 respectively. The systematic uncertainties for the polarization as the function of  $z$   
 495 and  $j_T$  are estimated with the same procedure.



$\Lambda$							
jet $p_T$ [GeV]	$P_\Lambda$	$\sigma_{\text{stat}}$	$\sigma_{\text{bkg}}$	$\sigma_\alpha$	$\sigma_{\text{trig}}$	$\sigma_{\text{mixed}}$	$\sigma_{\text{sys}}$
6-7	-0.0098	0.0058	0.0007	0.0001	0.0009	0.0005	0.0012
7-8.4	-0.0089	0.0057	0.001	0.0001	0.0008	0.0004	0.0014
8.4-10	-0.0051	0.0038	0.0005	0.0001	0.0000	0.0003	0.0005
10-12	0.0025	0.0042	0.0012	0.0000	0.0007	0.0001	0.0014
12-14	-0.0002	0.0057	0.0004	0.0000	0.0002	0.0000	0.0005
14-18	0.0154	0.0065	0.001	0.0002	0.0021	0.0008	0.0025
18-50	0.0246	0.0113	0.0009	0.0003	0.003	0.0012	0.0033

Table 7.1: The table of  $\Lambda$  extracted polarization, statistical uncertainties and summary of systematic uncertainties at different jet  $p_T$  ranges

$\bar{\Lambda}$							
jet $p_T$ [GeV]	$P_{\bar{\Lambda}}$	$\sigma_{\text{stat}}$	$\sigma_{\text{bkg}}$	$\sigma_\alpha$	$\sigma_{\text{trig}}$	$\sigma_{\text{mixed}}$	$\sigma_{\text{sys}}$
6-7	-0.0165	0.0052	0.0007	0.0001	0.0015	0.0008	0.0019
7-8.4	0.0028	0.0056	0.001	0.0000	0.0005	0.0002	0.0012
8.4-10	-0.0125	0.0037	0.0005	0.0001	0.0001	0.0006	0.0008
10-12	-0.0057	0.0045	0.0012	0.0000	0.0009	0.0003	0.0015
12-14	-0.0208	0.0063	0.0004	0.0001	0.0008	0.001	0.0014
14-18	-0.0104	0.0075	0.001	0.0001	0.0015	0.0006	0.0019
18-50	-0.0299	0.0134	0.0009	0.0002	0.0036	0.0015	0.0040

Table 7.2: The table of  $\bar{\Lambda}$  extracted polarization, statistical uncertainties and summary of systematic uncertainties at different jet  $p_T$  ranges

496 **8 Results and conclusion**

497 In this analysis, we measure the dependence of  $\Lambda$  and  $\bar{\Lambda}$  transverse polarization on jet  $p_T$ ,  $z$  and  
 498  $j_T$ .

499 **8.1  $P_{\Lambda/\bar{\Lambda}}$  vs jet  $p_T$**

500 Figure 8.1 shows the results of transverse polarization of  $\Lambda$  as a function of jet  $p_T$ . The red and  
 501 blue markers denote  $\Lambda$  and  $\bar{\Lambda}$  respectively. We can observe the significant transverse polarization  
 502 of both  $\Lambda$  and  $\bar{\Lambda}$  and clear jet  $p_T$  dependence. The  $\Lambda$  polarization increases with jet  $p_T$  and  
 503 changes its sign from negative to positive at jet  $p_T \sim 12$  GeV. The  $\bar{\Lambda}$  polarization also increases  
 504 with jet  $p_T$  but is always negative. In this figure, the vertical bars denote statistical uncertain-  
 505 ties, and open boxes denote systematic uncertainties. The numerical values of the results are  
 506 summarized in Tab. 8.1.

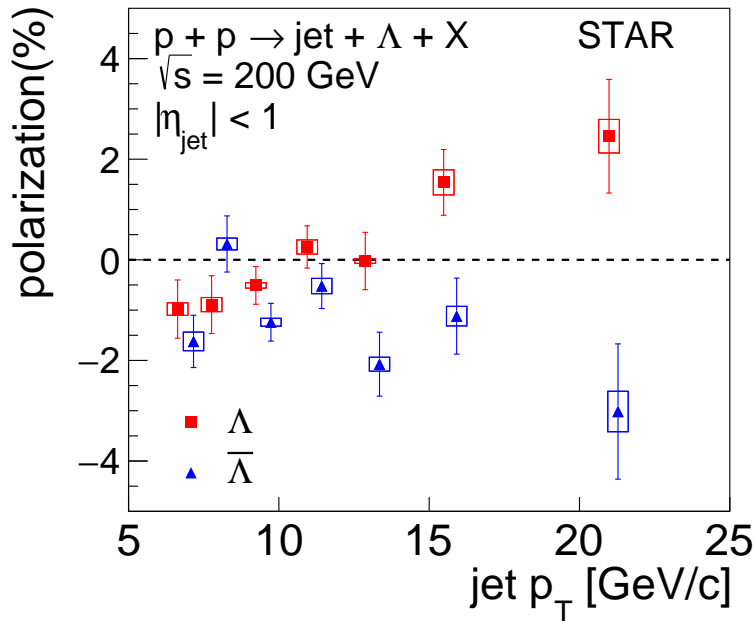


Figure 8.1: Transverse polarization of  $\Lambda$  and  $\bar{\Lambda}$  as a function of jet  $p_T$  in unpolarized  $pp$  collisions at  $\sqrt{s} = 200$  GeV at STAR. Statistical uncertainties are shown as vertical bars. Systematic uncertainties are shown as boxes.

507 **8.2  $P_{\Lambda/\bar{\Lambda}}$  vs  $z$  and  $j_T$**

508 To provide further constraints for the pFFs, the transverse polarizations of  $\Lambda$  and  $\bar{\Lambda}$  are also  
 509 measured as functions of  $z$  and  $j_T$ , as shown in Figure 8.2 and 8.3. Because the  $\Lambda$  polarization  
 510 as a function of jet  $p_T$  cross zero from negative to positive. There might be different  $z$  and  
 511  $j_T$  dependence of polarization at different jet  $p_T$  ranges. Hence, We separate jet  $p_T$  into three  
 512 different ranges of:  $6 < p_T^{jet} < 8.4$  GeV,  $8.4 < p_T^{jet} < 12$  GeV and  $p_T^{jet} > 12$  GeV, respectively.  
 513 The polarizations of  $\Lambda$  and  $\bar{\Lambda}$  show different  $z$  dependence at different jet  $p_T$  ranges. At low jet  
 514  $p_T$  range of  $6 < p_T^{jet} < 8.4$  GeV, no clear  $z$  dependence of  $\Lambda$  or  $\bar{\Lambda}$  polarization is observed. The  
 515 polarization trend with  $z$  of  $\Lambda$  is similar to  $\bar{\Lambda}$  at  $8.4 < p_T^{jet} < 12$  GeV range. At high jet  $p_T$

jet $p_T$ [GeV]	$\Lambda$			jet $p_T$ [GeV]	$\bar{\Lambda}$		
	$P_\Lambda$	$\sigma_{\text{stat}}$	$\sigma_{\text{sys}}$		$P_{\bar{\Lambda}}$	$\sigma_{\text{stat}}$	$\sigma_{\text{sys}}$
6.4821	-0.0098	0.0058	0.0012	6.47	-0.0165	0.0052	0.0019
7.6453	-0.0089	0.0057	0.0014	7.627	0.0028	0.0056	0.0012
9.1596	-0.0051	0.0038	0.0005	9.1422	-0.0125	0.0037	0.0008
10.9155	0.0025	0.0042	0.0014	10.8958	-0.0057	0.0045	0.0015
12.9024	-0.0002	0.0057	0.0005	12.8898	-0.0208	0.0063	0.0014
15.586	0.0154	0.0065	0.0025	15.5532	-0.0104	0.0075	0.0019
21.2445	0.0246	0.0113	0.0033	21.1216	-0.0299	0.0134	0.0040

Table 8.1: The table of  $\Lambda$  and  $\bar{\Lambda}$  extracted polarization, statistical uncertainties and summary of systematic uncertainties at different jet  $p_T$  ranges

516 range, the polarization of  $\Lambda$  and  $\bar{\Lambda}$  become opposite and increase with  $z$ . But no  $j_T$  dependence  
517 of polarization is observed at these three jet  $p_T$  range.

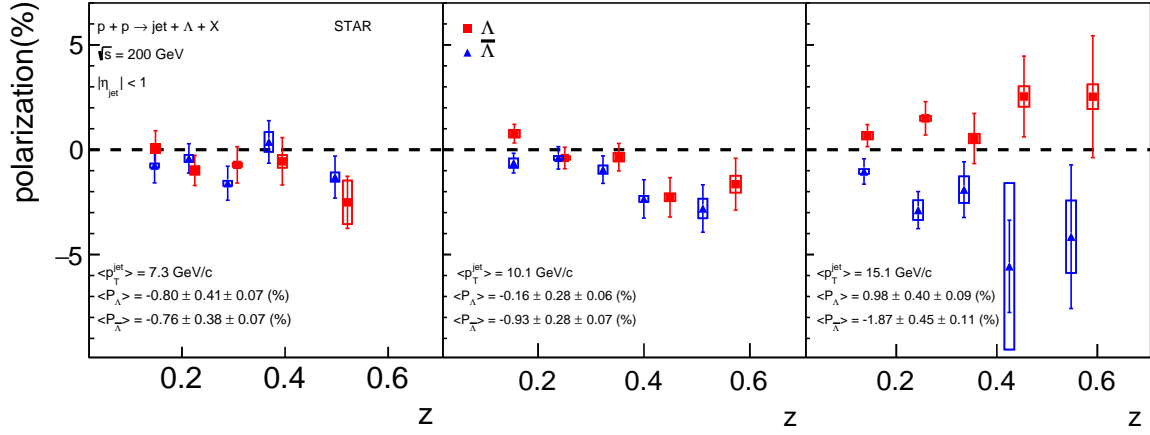


Figure 8.2: Transverse polarization of  $\Lambda$ , and  $\bar{\Lambda}$  as a function of  $z$  at different jet  $p_T$  ranges of  $6 < p_T^{\text{jet}} < 8.4 \text{ GeV}$  (left),  $8.4 < p_T^{\text{jet}} < 12 \text{ GeV}$  (middle) and  $p_T^{\text{jet}} > 12 \text{ GeV}$  (right). Statistical uncertainties are shown as vertical bars. Systematic uncertainties are shown as boxes.

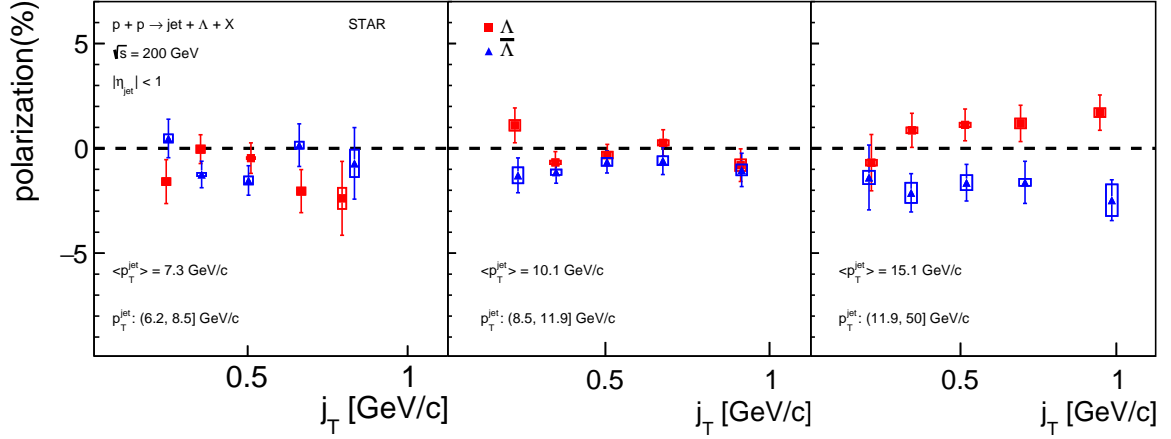


Figure 8.3: Transverse polarization of  $\Lambda$ , and  $\bar{\Lambda}$  as a function of  $j_T$  at different jet  $p_T$  ranges of  $6 < p_T^{jet} < 8.4$  GeV (left),  $8.4 < p_T^{jet} < 12$  GeV (middle) and  $p_T^{jet} > 12$  GeV (right). Statistical uncertainties are shown as vertical bars. Systematic uncertainties are shown as boxes.

$6 < p_T^{jet} \leq 8.4$				$8.4 < p_T^{jet} \leq 12$				$p_T^{jet} > 12$			
$z$	$P_\Lambda$	$\sigma_{stat}$	$\sigma_{sys}$	$z$	$P_\Lambda$	$\sigma_{stat}$	$\sigma_{sys}$	$z$	$P_\Lambda$	$\sigma_{stat}$	$\sigma_{sys}$
0.1528	0.0006	0.0085	0.0022	0.1426	0.0077	0.0044	0.0018	0.1243	0.0067	0.0053	0.0018
0.2484	-0.0099	0.0072	0.0020	0.2449	-0.004	0.0051	0.0008	0.2463	0.015	0.008	0.0012
0.3448	-0.0072	0.0087	0.0009	0.3459	-0.0036	0.0065	0.002	0.3432	0.0053	0.012	0.0023
0.4457	-0.0056	0.0113	0.003	0.4434	-0.0227	0.0094	0.0019	0.4424	0.0254	0.0193	0.0049
0.6033	-0.0251	0.0124	0.0103	0.5926	-0.0164	0.0124	0.0040	0.5908	0.0253	0.0291	0.0059
$z$	$P_{\bar{\Lambda}}$	$\sigma_{stat}$	$\sigma_{sys}$	$z$	$P_{\bar{\Lambda}}$	$\sigma_{stat}$	$\sigma_{sys}$	$z$	$P_{\bar{\Lambda}}$	$\sigma_{stat}$	$\sigma_{sys}$
0.157	-0.0076	0.0083	0.0010	0.1229	0.0035	0.0019	0.0022	0.1251	-0.0104	0.0061	0.0011
0.2491	-0.0042	0.007	0.0017	0.247	-0.0017	0.003	0.0009	0.2463	-0.0288	0.0088	0.0047
0.3458	-0.016	0.0081	0.0012	0.3454	0.0001	0.0043	0.0020	0.343	-0.019	0.0133	0.0063
0.4464	0.0037	0.0101	0.0047	0.4445	-0.0023	0.0064	0.0014	0.442	-0.0556	0.022	0.0397
0.6198	-0.013	0.01	0.0022	0.6065	-0.0044	0.0074	0.0047	0.6071	-0.0415	0.0343	0.0172

Table 8.2: The table of  $\Lambda$  and  $\bar{\Lambda}$  extracted polarization, statistical uncertainties and summary of systematic uncertainties at different  $z$  ranges

### 518 8.3 Conclusions

- 519 • Our analysis is the first measurement of transverse polarization of  $\Lambda$  and  $\bar{\Lambda}$  within jet in  
520 unpolarized  $pp$  collisions at  $\sqrt{s} = 200$  GeV.
- 521 • Significant polarizations of  $\Lambda$  and  $\bar{\Lambda}$  are observed with clear dependence on jet  $p_T$ .
- 522 • The  $z$  and  $j_T$  dependence of polarization are measured, and visible  $z$  dependencies are  
523 observed for medium to high jet  $p_T$ .
- 524 • These measurements provide important constraints on polarizing Fragmentation Func-  
525 tions.

$6 < p_T^{jet} \leq 8.4$				$8.4 < p_T^{jet} \leq 12$				$p_T^{jet} > 12$			
$j_T$	$P_\Lambda$	$\sigma_{stat}$	$\sigma_{sys}$	$j_T$	$P_\Lambda$	$\sigma_{stat}$	$\sigma_{sys}$	$j_T$	$P_\Lambda$	$\sigma_{stat}$	$\sigma_{sys}$
0.1345	-0.0159	0.0105	0.0016	0.136	0.011	0.0083	0.0025	0.1381	-0.0068	0.0134	0.0014
0.2993	-0.0004	0.0069	0.0018	0.3006	-0.0067	0.0052	0.0009	0.3014	0.0086	0.0081	0.0014
0.49	-0.0047	0.0073	0.0004	0.4926	-0.0032	0.0051	0.0016	0.494	0.0112	0.0076	0.0010
0.6821	-0.0204	0.0103	0.0017	0.6873	0.0026	0.0063	0.0012	0.6901	0.0119	0.0087	0.0023
0.9026	-0.0238	0.0176	0.0050	0.9506	-0.008	0.0078	0.0028	1.006	0.017	0.0084	0.0021
$j_T$	$\overline{P}_\Lambda$	$\sigma_{stat}$	$\sigma_{sys}$	$j_T$	$\overline{P}_\Lambda$	$\sigma_{stat}$	$\sigma_{sys}$	$j_T$	$\overline{P}_\Lambda$	$\sigma_{stat}$	$\sigma_{sys}$
0.1349	0.0047	0.0092	0.0019	0.1366	-0.0129	0.0083	0.0038	0.1376	-0.0139	0.0155	0.0032
0.2985	-0.0125	0.0063	0.0008	0.3009	-0.0114	0.0053	0.0013	0.3023	-0.0212	0.0091	0.0048
0.4898	-0.0153	0.007	0.0019	0.4928	-0.0065	0.0053	0.0019	0.4947	-0.0164	0.0087	0.0036
0.6831	0.0015	0.0102	0.0017	0.6882	-0.0059	0.0066	0.0021	0.6909	-0.0162	0.01	0.0017
0.9057	-0.0072	0.0171	0.0065	0.9597	-0.0103	0.0079	0.0026	1.0123	-0.0247	0.0097	0.0075

Table 8.3: The table of  $\Lambda$  and  $\overline{\Lambda}$  extracted polarization, statistical uncertainties and summary of systematic uncertainties at different  $z$  ranges

526 **References**

- 527 [1] T. D. Lee and C. N. Yang, Phys. Rev. **108**, 1645 (1957).  
528 [2] M. I. Abdulhamid et al. [STAR collaboration], Phys. Rev. D **109**, 012004 (2024) Ming Shao  
529 et al. PRC 75, 064901 (2007)  
530 [3] Ming Shao et al. Phys. Rev. C **75**, 064901 (2007)  
531 [4] B. Abelev et al. [ALICE Collaboration], Phys. Rev. D **91**, 112012 (2015).  
532 [5] M. Cacciari, G. P. Salam, and G. Soyez, Eur. Phys. J. C **72**, 1896 (2012).  
533 [6] T. Sjostrand, S. Mrenna and P.Z. Skands, PYTHIA 64 physics and manual, JHEP 05 026  
534 (2006).  
535 [7] R Brun et al. Report No.CERN-DD-EE-84-1 (1987)  
536 [8] S.F. Pate et al. JINST **18** P10032 (2023)  
537 [9] Zyla, P.A., et al. [Particle Data Group], The Review of Particle Physics, Phys. Rev. D **110**,  
538 030001 (2024)

# Appendices

540	16042102	16045032	16046016	16048002	16050070	16052022	16053065	16055127	16058080
541	16060042	16062018	16042103	16045033	16046017	16048003	16050071	16052023	16053066
542	16055128	16058082	16060043	16062019	16042105	16045043	16046018	16048004	16050072
543	16052028	16053067	16055129	16058083	16060044	16062020	16042116	16045044	16046019
544	16048009	16050073	16052030	16053073	16055130	16058084	16060045	16062021	16042117
545	16045045	16046020	16048014	16050075	16052031	16053074	16055131	16058085	16060046
546	16062022	16042118	16045047	16046021	16048015	16050076	16052032	16053075	16055132
547	16058086	16060053	16062023	16042126	16045048	16046032	16048016	16051001	16052034
548	16053077	16055133	16058087	16060054	16062024	16043002	16045049	16046033	16048017
549	16051003	16052035	16053078	16055134	16058088	16060055	16062025	16043004	16045052
550	16046034	16048018	16051004	16052036	16053079	16056004	16058089	16060056	16062045
551	16043006	16045054	16046035	16048019	16051007	16052037	16054001	16056016	16058090
552	16060057	16062046	16043007	16045055	16046036	16048022	16051008	16052038	16054005
553	16056017	16058091	16060058	16062047	16043009	16045056	16046037	16048023	16051009
554	16052039	16054006	16056018	16058093	16060059	16062049	16043013	16045067	16046038
555	16048024	16051022	16052040	16054007	16056019	16058095	16060060	16062050	16043016
556	16045068	16046039	16048025	16051026	16052041	16054010	16056022	16058096	16060061
557	16062051	16043019	16045070	16046040	16048026	16051027	16052042	16054011	16056023
558	16058100	16060062	16062052	16043020	16045082	16046041	16048027	16051028	16052043
559	16054012	16057003	16059011	16060063	16062053	16043021	16045083	16046042	16048028
560	16051029	16052044	16054013	16057004	16059012	16060064	16062054	16043022	16045084
561	16046043	16048109	16051030	16052045	16054014	16057005	16059013	16060065	16062055
562	16043024	16045085	16046044	16048110	16051031	16052046	16054018	16057006	16059015
563	16061008	16062056	16043026	16045086	16046045	16048111	16051032	16052048	16054019
564	16057007	16059016	16061009	16062057	16043031	16045087	16046046	16048115	16051033
565	16052049	16054020	16057008	16059017	16061010	16062058	16043033	16045088	16046048
566	16048116	16051034	16052050	16054022	16057009	16059018	16061011	16062078	16043035
567	16045089	16046049	16048117	16051035	16052051	16054059	16057010	16059019	16061012
568	16063001	16043037	16045090	16046050	16048118	16051036	16052087	16054060	16057011
569	16059022	16061013	16063002	16043079	16045093	16046057	16048119	16051037	16052088
570	16054061	16057012	16059024	16061014	16063003	16043082	16045094	16046058	16048120
571	16051038	16052089	16054062	16057013	16059025	16061015	16063004	16043084	16045095
572	16046059	16048121	16051039	16053001	16054063	16057016	16059026	16061016	16063005
573	16043085	16045096	16046061	16048122	16051040	16053002	16054064	16057017	16059027
574	16061017	16063006	16043086	16045097	16046062	16048125	16051041	16053003	16054069
575	16057018	16059030	16061018	16063007	16043089	16045098	16046064	16048126	16051042
576	16053004	16054070	16057046	16059031	16061019	16063091	16043091	16045099	16046065
577	16048127	16051044	16053005	16054072	16057047	16059041	16061035	16063092	16043092
578	16045100	16046066	16048128	16051045	16053006	16054073	16057048	16059062	16061037
579	16063093	16043096	16045102	16046067	16049010	16051046	16053007	16054074	16057049
580	16059064	16061038	16063094	16043105	16045103	16046073	16049012	16051047	16053008
581	16054075	16057050	16059065	16061039	16063095	16043106	16045104	16046074	16049013
582	16051048	16053009	16054077	16057051	16059066	16061041	16063096	16044017	16045105
583	16046075	16049017	16051049	16053010	16054078	16057053	16059067	16061042	16063097
584	16044019	16045106	16046076	16049018	16051050	16053011	16054079	16058001	16059068

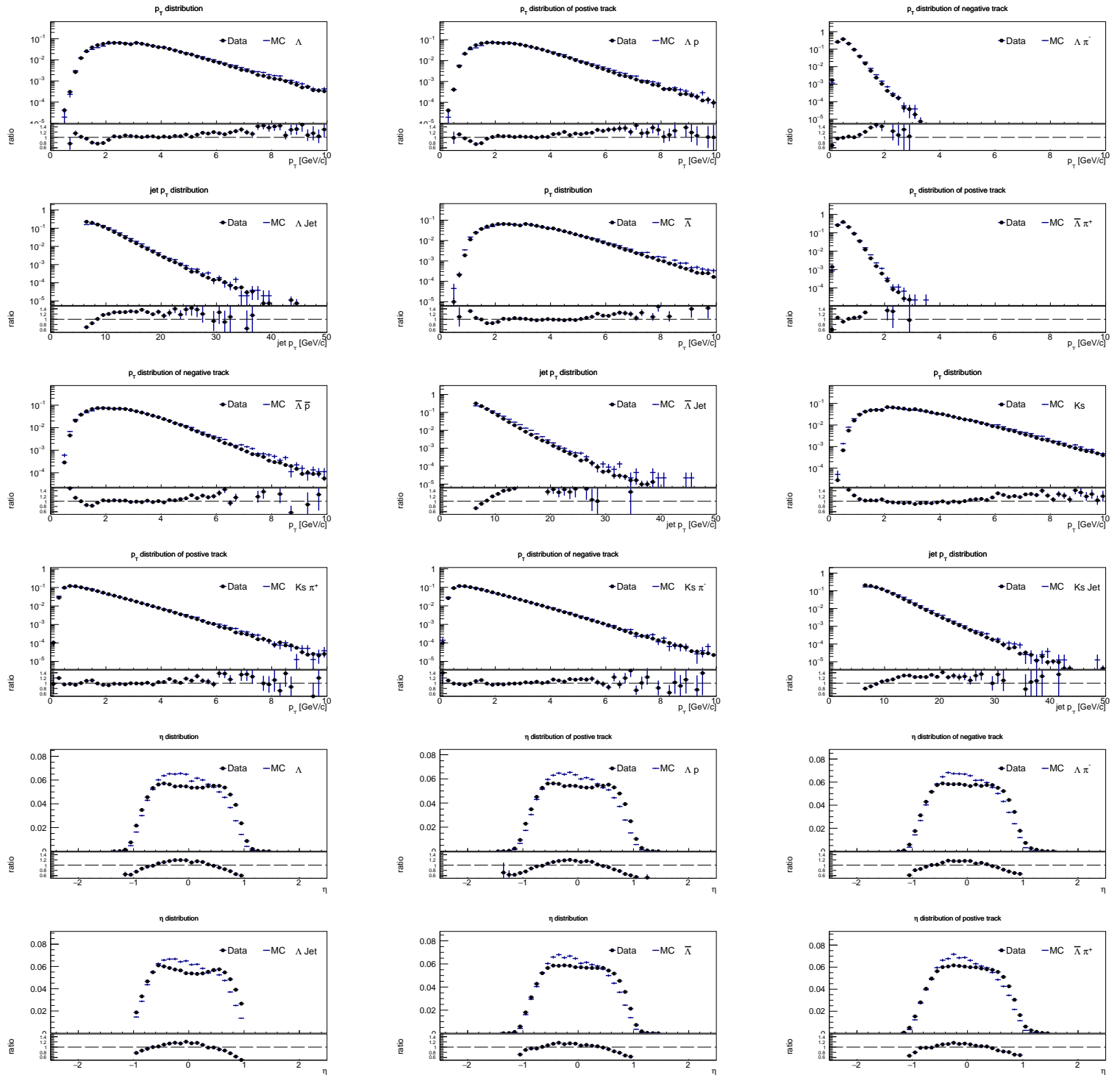
585 16061049 16063099 16044022 16045108 16046077 16049020 16051051 16053012 16054080  
586 16058002 16059069 16061060 16063100 16044023 16045109 16046078 16049022 16051052  
587 16053017 16054082 16058005 16060001 16061061 16063111 16044027 16045110 16046080  
588 16049023 16051056 16053019 16054086 16058006 16060002 16061062 16063112 16044028  
589 16045111 16046081 16049024 16051057 16053030 16054087 16058007 16060003 16061075  
590 16063113 16044029 16045112 16046082 16049025 16051058 16053031 16055002 16058008  
591 16060004 16061076 16064001 16044030 16045113 16046083 16050009 16051059 16053043  
592 16055003 16058015 16060005 16061077 16064002 16044033 16045114 16047004 16050010  
593 16051060 16053044 16055004 16058016 16060008 16061078 16064006 16044036 16045115  
594 16047005 16050036 16051101 16053045 16055005 16058017 16060011 16061083 16064007  
595 16044037 16045116 16047008 16050037 16051102 16053046 16055007 16058018 16060014  
596 16061084 16064008 16044038 16045117 16047101 16050038 16051103 16053047 16055010  
597 16058019 16060016 16062001 16064009 16044046 16045118 16047102 16050039 16051104  
598 16053048 16055011 16058020 16060017 16062002 16064010 16044047 16045119 16047103  
599 16050040 16051105 16053049 16055012 16058021 16060018 16062003 16064013 16044050  
600 16045120 16047104 16050041 16051106 16053051 16055013 16058022 16060026 16062004  
601 16064017 16044061 16046003 16047106 16050042 16051107 16053052 16055018 16058023  
602 16060027 16062005 16064018 16044110 16046005 16047108 16050043 16051108 16053053  
603 16055019 16058024 16060028 16062006 16064019 16044111 16046006 16047121 16050044  
604 16051109 16053054 16055021 16058025 16060030 16062008 16044112 16046007 16047122  
605 16050048 16051110 16053055 16055022 16058026 16060031 16062009 16044114 16046008  
606 16047124 16050049 16051111 16053056 16055024 16058070 16060032 16062010 16044115  
607 16046009 16047125 16050050 16052013 16053057 16055025 16058071 16060034 16062011  
608 16044120 16046010 16047126 16050051 16052015 16053058 16055120 16058072 16060036  
609 16062012 16044123 16046011 16047131 16050052 16052016 16053059 16055121 16058073  
610 16060037 16062013 16044133 16046012 16047136 16050053 16052017 16053060 16055122  
611 16058074 16060038 16062014 16044138 16046013 16047137 16050054 16052018 16053062  
612 16055123 16058077 16060039 16062015 16044139 16046014 16047138 16050065 16052019  
613 16053063 16055124 16058078 16060040 16062016 16045001 16046015 16048001 16050066  
614 16052021 16053064 16055125 16058079 16060041 16062017  
  
615 16065023 16067016 16069064 16073013 16078041 16080043 16082050 16085032 16087021  
616 16089020 16091009 16065024 16067017 16069065 16073017 16078042 16080045 16082051  
617 16085033 16087022 16089024 16091010 16065025 16067019 16069067 16073018 16078056  
618 16080046 16082052 16085035 16087023 16089026 16091011 16065026 16067020 16070003  
619 16073019 16079001 16080047 16082053 16085036 16087024 16089027 16091012 16065027  
620 16067021 16070004 16073020 16079010 16080048 16082054 16085037 16087025 16089028  
621 16091013 16065028 16067022 16070005 16073021 16079011 16080049 16082055 16085051  
622 16087026 16089029 16091014 16065036 16067040 16070006 16073029 16079013 16080050  
623 16082056 16085052 16087027 16089030 16091061 16065037 16067041 16070008 16073030  
624 16079014 16080051 16082057 16085054 16087028 16089031 16091062 16065038 16067042  
625 16070009 16073031 16079015 16080052 16083005 16085055 16087029 16089041 16091063  
626 16065039 16067043 16070010 16073032 16079016 16080053 16083006 16085056 16087030  
627 16089042 16092001 16065041 16067044 16070012 16073033 16079017 16080054 16083007  
628 16085057 16087031 16089043 16092002 16065042 16068001 16070013 16073034 16079018  
629 16080055 16083008 16085058 16087032 16089044 16092003 16065044 16068003 16070014  
630 16073035 16079019 16081001 16083009 16085061 16087033 16089045 16092015 16065045  
631 16068004 16071016 16073037 16079020 16081002 16083010 16085062 16087042 16089046

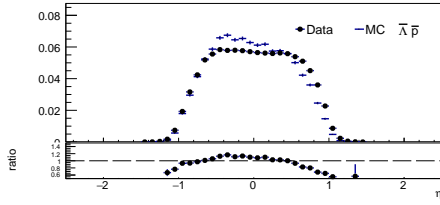
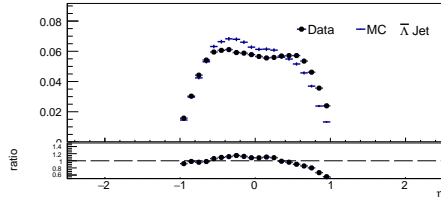
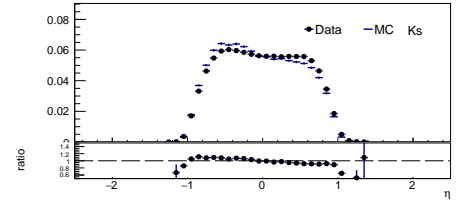
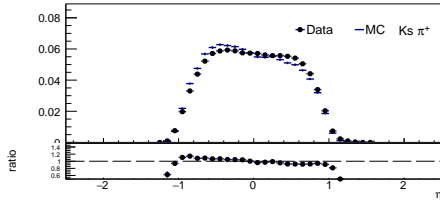
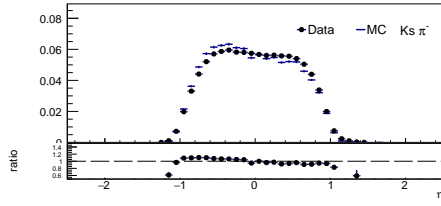
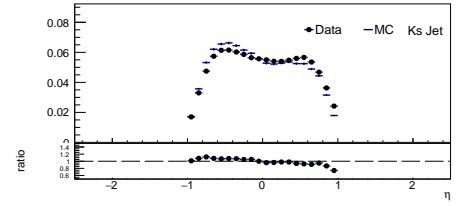
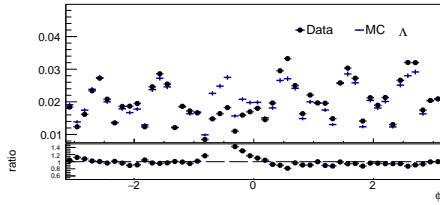
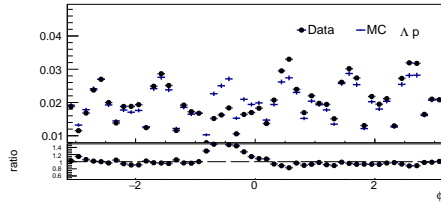
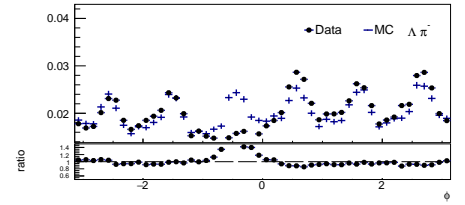
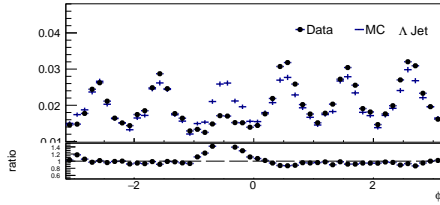
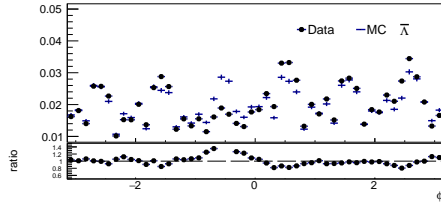
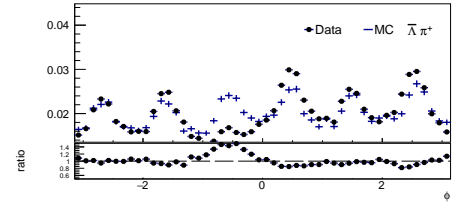
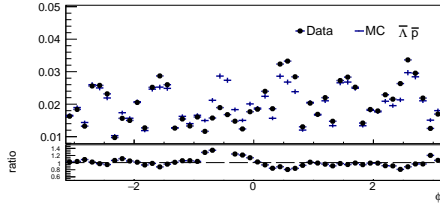
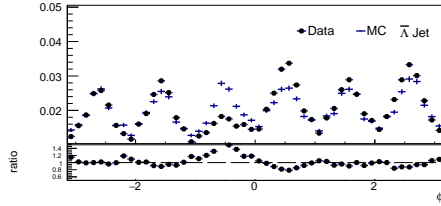
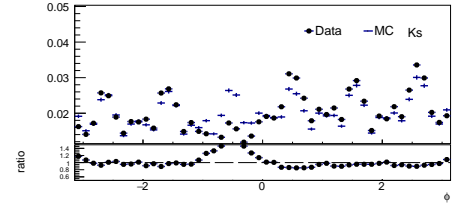
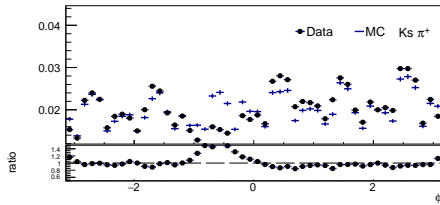
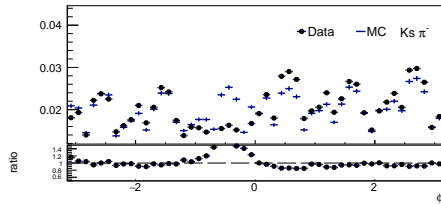


632 16092016 16065046 16068005 16071050 16073038 16079021 16081003 16083011 16085065  
633 16087043 16089047 16092017 16065047 16068006 16071051 16073039 16079022 16081012  
634 16083012 16085067 16087044 16089048 16092018 16065048 16068007 16071052 16073040  
635 16079023 16081013 16083013 16085069 16087045 16089049 16092019 16065060 16068008  
636 16071053 16073045 16079024 16081015 16083014 16085071 16087046 16089050 16092020  
637 16065061 16068009 16071054 16073046 16079027 16081016 16083015 16085072 16087047  
638 16089051 16092021 16065072 16068010 16071055 16073047 16079028 16081017 16083016  
639 16085073 16087048 16089052 16092022 16066001 16068013 16071056 16073048 16079029  
640 16081018 16083017 16085074 16087049 16089053 16092023 16066002 16068014 16071058  
641 16073049 16079030 16081019 16083018 16086001 16087050 16089054 16092033 16066003  
642 16068015 16071059 16073050 16079031 16081020 16083019 16086002 16087051 16090001  
643 16092034 16066004 16068016 16071060 16077021 16079032 16081021 16083042 16086003  
644 16087052 16090002 16092035 16066005 16068017 16071061 16077027 16079033 16081022  
645 16083043 16086004 16087053 16090003 16092036 16066006 16068018 16071076 16077028  
646 16079034 16081024 16083044 16086005 16087054 16090004 16092037 16066007 16068021  
647 16071077 16077029 16079035 16081025 16083045 16086006 16087055 16090005 16092042  
648 16066008 16068022 16071078 16077030 16079036 16081036 16083046 16086007 16088001  
649 16090015 16092044 16066009 16068023 16071079 16077031 16079046 16081037 16083048  
650 16086008 16088016 16090016 16092048 16066011 16068024 16072001 16077032 16079047  
651 16081048 16083049 16086025 16088017 16090017 16092049 16066012 16068025 16072002  
652 16077033 16079048 16081049 16083050 16086026 16088018 16090018 16092050 16066015  
653 16068028 16072003 16077034 16079049 16081050 16083052 16086027 16088019 16090019  
654 16092051 16066016 16068029 16072006 16077037 16079052 16081052 16083053 16086028  
655 16088020 16090020 16092052 16066017 16068030 16072007 16077038 16079054 16081053  
656 16083055 16086030 16088021 16090021 16092053 16066018 16068032 16072008 16077039  
657 16079057 16081054 16083056 16086031 16088022 16090022 16092054 16066019 16068034  
658 16072009 16077040 16079058 16081055 16083057 16086032 16088023 16090023 16092055  
659 16066020 16068035 16072010 16077041 16079059 16081056 16083058 16086033 16088025  
660 16090024 16092063 16066021 16068036 16072012 16077043 16079060 16081057 16083059  
661 16086034 16088026 16090025 16092064 16066026 16068037 16072013 16077047 16079061  
662 16081058 16083060 16086035 16088027 16090026 16092065 16066027 16068038 16072014  
663 16078002 16079062 16081059 16084004 16086036 16088028 16090027 16092066 16066030  
664 16068039 16072022 16078003 16079063 16081060 16084006 16086037 16088029 16090028  
665 16092067 16066031 16068040 16072023 16078004 16080002 16081061 16084007 16086038  
666 16088030 16090029 16092068 16066032 16068042 16072024 16078005 16080004 16082001  
667 16084008 16086039 16088031 16090030 16092070 16066033 16068056 16072025 16078006  
668 16080005 16082002 16084009 16086040 16088040 16090038 16092071 16066035 16068057  
669 16072026 16078008 16080006 16082012 16084011 16086041 16088041 16090039 16093001  
670 16066047 16068058 16072033 16078009 16080012 16082013 16084012 16086042 16088042  
671 16090041 16093002 16066049 16069001 16072034 16078010 16080013 16082017 16084013  
672 16086051 16088043 16090042 16093003 16066050 16069002 16072035 16078011 16080014  
673 16082018 16084014 16086052 16088044 16090044 16093004 16066051 16069003 16072036  
674 16078013 16080015 16082019 16084015 16086053 16088045 16090045 16093011 16066052  
675 16069004 16072038 16078014 16080020 16082022 16085008 16086054 16088046 16090046  
676 16093012 16066053 16069005 16072039 16078028 16080021 16082023 16085009 16087001  
677 16088047 16090047 16093013 16066054 16069006 16072040 16078029 16080022 16082025  
678 16085011 16087002 16088048 16090048 16093014 16066055 16069007 16072041 16078030  
679 16080023 16082027 16085012 16087003 16088049 16090049 16093015 16066059 16069009

680 16072042 16078031 16080024 16082028 16085013 16087004 16088050 16090050 16093016  
681 16066060 16069010 16072043 16078032 16080025 16082029 16085014 16087005 16089001  
682 16090051 16093017 16067001 16069011 16072058 16078033 16080026 16082039 16085024  
683 16087006 16089002 16090052 16093018 16067003 16069012 16072059 16078034 16080027  
684 16082040 16085025 16087007 16089003 16090053 16067004 16069016 16072060 16078035  
685 16080028 16082041 16085026 16087008 16089004 16091003 16067005 16069053 16072061  
686 16078036 16080029 16082042 16085027 16087009 16089005 16091004 16067006 16069054  
687 16072062 16078037 16080030 16082043 16085028 16087010 16089016 16091005 16067013  
688 16069055 16073001 16078038 16080031 16082046 16085029 16087011 16089017 16091006  
689 16067014 16069062 16073010 16078039 16080032 16082047 16085030 16087019 16089018  
690 16091007 16067015 16069063 16073012 16078040 16080033 16082048 16085031 16087020  
691 16089019 16091008  
  
692 16094016 16094019 16094020 16094021 16094022 16094025 16094026 16094027  
693 16094028 16094029 16094030 16094032 16094033 16094034 16094035 16094048  
694 16094049 16094050 16094051 16094052 16094053 16094054 16095006 16095007  
695 16095008 16095019 16095020 16095028 16095029 16095030 16095031 16095032  
696 16095033 16095035 16095038 16095039 16095041 16095042 16095043 16095044  
697 16095045 16095046 16096053 16096054 16096062 16096063 16096064 16096065  
698 16096066 16096067 16096068 16096069 16097001 16097002 16097003 16097004  
699 16097005 16097006 16097007 16097008 16097009 16097011 16097012 16097013  
700 16097015 16097016 16097030 16097031 16097032 16097033 16097035 16097036  
701 16097037 16097038 16097039 16097042 16097044 16097045 16097049 16097050  
702 16097057 16097058 16097059 16097064 16097065 16097066 16098001 16098002  
703 16098003 16098004 16098008 16098009 16098010 16098011 16098027 16099002  
704 16099003 16099004 16099005 16099006 16099007 16099008 16099009 16099010  
705 16099011 16099012 16099013 16099014 16099026 16099027 16099028 16099029  
706 16099030 16099042 16099043 16099046 16099048 16099049 16099050 16099051  
707 16099053 16099054 16099055 16099056 16099057 16099059 16099060 16099061  
708 16100052 16100053 16100054 16100055 16100056 16100069 16100070 16100072  
709 16100073 16100074 16100077 16100078 16100079 16100080 16100081 16100082  
710 16100083 16100084 16100085 16100086 16100088 16101002 16101003 16101012  
711 16101013 16101014 16101016 16101019 16101020 16101034 16101035 16101036  
712 16101037 16101038 16101039 16101040 16101041 16101042 16101043 16101044  
713 16101045 16101046 16101047 16101048 16101057 16101058 16102001 16102002  
714 16102003 16102004 16102005 16102007 16102010 16102012 16102014 16102015  
715 16102016 16102017 16102018 16102019 16102020 16102033 16102034 16102035  
716 16102036 16102038 16102039 16102040 16102041 16102042 16102043 16102044  
717 16102045 16102046 16102047 16102048 16102053 16102054 16102055 16102056  
718 16102058 16102061 16102062 16102063 16102064 16102065 16102066 16103002  
719 16103003 16103005 16103006 16103007 16103008 16103009 16103010 16103011  
720 16103012 16103013 16103014 16103015 16103016 16103017 16103018 16103029  
721 16103031 16103032 16103033 16103034 16103035 16103038 16103039 16103041  
722 16103042 16103043 16103044 16103045 16103046 16103047 16103048 16103051  
723 16103052 16104010 16104011 16104015 16104016 16104017 16104018 16104019  
724 16104020 16104021 16104023 16104025 16104027 16104029 16104031 16104034  
725 16104035 16104044 16104045 16104046 16104047 16104049 16104050 16104051  
726 16104052 16104053 16104054 16104055 16104056 16104057 16104059 16104060

727 16105038 16105039 16105040 16105041 16105042 16105045 16105046 16106002  
728 16106003 16106004 16106005 16106006 16106007 16106008 16106009 16106016  
729 16106017 16106018 16106019 16106020 16106021 16106045 16106048 16106049  
730 16106050 16106051 16106052 16106053 16106054 16106058 16107007 16107010  
731 16107012 16107013 16107014 16107015 16107016 16107018 16107020 16107021  
732 16107022 16107047 16107052 16107055 16107058 16107060 16107061 16107062  
733 16107063 16108001 16108002 16108003 16108004 16108005 16108010 16108011  
734 16108013 16108017 16108018 16108019 16108020 16108028 16108033 16108035  
735 16108036 16108039 16108044 16108056 16108057 16108058 16109001 16109023  
736 16109025 16109026 16109031 16109032 16109033 16109034 16109035 16109037  
737 16109038 16109049 16109050 16109051 16109052 16109053 16109054 16109056  
738 16109057 16109058 16109059 16109060 16109061 16110001 16110002 16110009  
739 16110010 16110011 16110012 16110013 16110014 16110015 16110016 16110017  
740 16110018 16110019 16110020 16110021 16110035 16110036 16110038 16110039  
741 16110040 16110041 16110042 16111001 16111002 16111005 16111025 16111026  
742 16111027 16111028 16111029 16111030 16111031 16111032 16111033 16111034  
743 16111036 16111037 16111038 16111039 16111040 16111041 16111042 16111043  
744 16111049 16111050 16112001 16112002 16112003 16112004 16112005 16112006  
745 16112007 16112008 16112009 16112010 16112011 16112012 16112013 16113003  
746 16113008 16113010 16113011 16113012 16113014 16113015 16113016 16113017  
747 16113019 16113020 16113021 16113022 16113028 16113029 16113040 16113041  
748 16113042 16113043 16113044 16113045 16113048 16113049 16113050 16113051  
749 16113052 16113053 16113055 16113056 16114002 16114003 16114004 16114005  
750 16114006 16114007 16114008 16114009 16114010 16114011 16114012 16114013  
751 16114014 16114015 16114016 16114017 16114018 16114026 16114027 16114028  
752 16114029 16114030 16114031 16114032 16114033 16114041 16114046 16114047  
753 16114048 16114049 16115001 16115002 16115029 16115030 16115033 16115034  
754 16115036 16115037 16115039 16115040 16115041 16115042 16115044 16115045  
755 16115046 16115047 16115048 16115054 16115055 16115056 16115057 16115058  
756 16115059 16115060 16115061 16115062 16115063 16115064 16115065 16115066  
757 16116001 16116002 16116007 16116008 16116009 16116010 16116011 16116033  
758 16116034 16116035 16116037 16116038 16116039 16116040 16116041 16116042  
759 16116043 16116044 16116045 16116046 16116047 16116053 16116054 16116055  
760 16117001 16117002 16117003 16117004 16117005 16117006 16117007 16117011  
761 16117012 16117014 16117017 16117018



$\eta$  distribution of negative track $\eta$  distribution $\eta$  distribution $\eta$  distribution of positive track $\eta$  distribution of negative track $\eta$  distribution $\phi$  distribution $\phi$  distribution of positive track $\phi$  distribution of negative track $\phi$  distribution $\phi$  distribution $\phi$  distribution of positive track $\phi$  distribution of negative track $\phi$  distribution $\phi$  distribution $\phi$  distribution of positive track $\phi$  distribution of negative track $\phi$  distribution